Cosmic spherules from Widerøefjellet, Sør Rondane Mountains (East Antarctica)

Steven Goderis [a,*], Bastien Soens [a], Matthew S. Huber [a,b], Seann McKibbin [a,c,d],
Matthias van Ginneken [e], Flore Van Maldeghem [a], Vinciane Debaille [f],
Richard C. Greenwood [g], Ian A. Franchi [g], Veerle Cnudde [h,i], Stijn Van Malderen [j],
Frank Vanhaecke [j], Christian Koeberl [k,l], Dan Topa [l], Philippe Claeys [a]

[a] Analytical-, Environmental-, and Geo-Chemistry, Vrije Universiteit Brussel, Pleinlaan 2, B-1050 Brussels, Belgium
[b] Department of Geology, University of the Free State, 205 Nelson Mandela Dr., Bloemfontein 9300, South Africa[1]
[c] Institut für Erd- und Umweltwissenschaften, Universität Potsdam, Haus 27, Karl-Liebknecht-Straße 24-25, Potsdam-Golm 14476, Germany[1]
[d] Geowissenschaftliches Zentrum, Abteilung Isotopengeologie, Georg-August-Universität Göttingen, Goldschmidtstraße 1,
Göttingen 37073, Germany[1]
[e] Royal Belgian Institute of Natural Sciences, 29 Rue Vautier, B-1000 Brussels, Belgium
[f] Laboratoire G-Time, Université Libre de Bruxelles 50, Av. F.D. Roosevelt CP 160/02, B-1050 Brussels, Belgium
[g] Planetary and Space Sciences, School of Physical Sciences, The Open University, Walton Hall, Milton Keynes MK7 6AA, United Kingdom
[h] Department of Geology, Ghent University, Campus Sterre, Krijgslaan 281 – S8, B-9000 Ghent, Belgium
[i] Department of Earth Sciences, Utrecht University, Princetonlaan 8a, 3584CB Utrecht, the Netherlands
[j] Department of Chemistry, Ghent University, Krijgslaan, 281 – S12, B-9000 Ghent, Belgium
[k] Department of Lithospheric Research, University of Vienna, Althanstrasse 14, A-1090 Vienna, Austria
[l] Natural History Museum, Burgring 7, A-1010 Vienna, Austria

Abstract

A newly discovered sedimentary accumulation of micrometeorites in the Sør Rondane Mountains of East Antarctica, close to the Widerøefjellet summit at ~2750 m above sea level, is characterized in this work. The focus here lies on 2099 melted cosmic spherules larger than 200 μm, extracted from 3.2 kg of sampled sediment. Although the Widerøefjellet deposit shares similarities to the micrometeorite traps encountered in the Transantarctic Mountains, both subtle and more distinct differences in the physicochemical properties of the retrieved extraterrestrial particles and sedimentary host deposits are discernable (e.g., types of bedrock, degree of wind exposure, abundance of metal-rich particles). Unlike the Frontier Mountain and Miller Butte sedimentary traps, the size fraction below 240 μm indicates some degree of sorting at Widerøefjellet, potentially through the redistribution by wind, preferential alteration of smaller particles, or processing biases. However, the cosmic spherules larger than 300 μm appear largely unbiased following their size distribution, frequency by textural type, and bulk chemical compositions. Based on the available bedrock exposure ages for the Sør Rondane Mountains, extraterrestrial dust is estimated to have accumulated over a time span of ~1–3 Ma at Widerøefjellet. Consequently, the Widerøefjellet collection reflects a substantial reservoir to sample the micrometeorite influx over this time interval. Petrographic observations and 3D microscopic CT imaging are combined with chemical and triple-oxygen isotopic analyses of silicate-rich cosmic spherules larger than 325 μm. The major element composition of 49 cosmic spherules confirms their principally chondritic parentage. For 18 glassy, 15 barred olivine, and 11 cryptocrystalline cosmic spherules, trace element concentrations are also reported on.

---

* Corresponding author.
  E-mail address: Steven.Goderis@vub.be (S. Goderis).
[1] Current address.

Based on comparison with evaporation experiments reported in literature and accounting for siderophile and chalcophile element losses during high-density phase segregation and ejection, the observed compositional sequence largely reflects progressive heating and evaporation during atmospheric passage accompanied by significant redox shifts, although the influence of (refractory) chondrite mineral constituents and terrestrial alteration cannot be excluded in all cases. Twenty-eight cosmic spherules larger than 325 μm analyzed for triple-oxygen isotope ratios confirm inheritance from mostly carbonaceous chondritic precursor materials (∼55% of the particles). Yet, ∼30% of the measured cosmic spherules and ∼50% of all glassy cosmic spherules are characterized by oxygen isotope ratios above the terrestrial fractionation line, implying genetic links to ordinary chondrites and parent bodies currently unsampled by meteorites. The structural, textural, chemical, and isotopic characteristics of the cosmic spherules from the Sør Rondane Mountains, and particularly the high proportion of Mg-rich glass particles contained therein, imply a well-preserved and representative new sedimentary micrometeorite collection from a previously unstudied region in East Antarctica characterized by distinct geological and exposure histories.

1. INTRODUCTION

Micrometeorites (MMs), dust particles within the size range of 10 μm–2 mm (Rubin and Grossman, 2010), dominate the 40,000 ± 20,000 metric tons of extraterrestrial matter accreting to Earth every year (Love and Brownlee, 1993). Due to different production mechanisms in and transportation pathways from their source regions, these microscopic particles sample parent bodies different from those of meteorites (e.g., Fredriksson and Martin, 1963; Ganapathy et al., 1978; Engrand and Maurette, 1998; Flynn et al., 2009; Gounelle et al., 2009; Dartois et al., 2013; Cordier and Folco, 2014; Rubin, 2018). Generally recovered from deep-sea sediments, seasonal lakes in Greenland, ice and snow in Greenland and Antarctica, Antarctic moraines, continental sands and soils, and more recently also urban environments (e.g., Brownlee et al., 1979; Blanchard et al., 1980; Koeberl and Hagen, 1989; Hagen et al., 1989; Engrand and Maurette, 1998; Taylor and Lever, 2001; Genge et al., 2016, 2017; Rudraswami et al., 2016; van Ginneken et al., 2017), MMs have also been found concentrated in high-altitude sedimentary traps, i.e., a pits, fissures and cracks of glacially eroded surfaces, in the Transantarctic Mountains (TAM) (e.g., Rochette et al., 2008; Suavet et al., 2009). To concentrate MMs in numbers sufficient to be able to efficiently distinguish them from terrestrial particles in sedimentary deposits, the accumulation time of such traps is ideally of the order of millions of years, while at the same time alteration must have remained limited, with minimal background or anthropogenic contributions (Suavet et al., 2009). In the case of the Antarctic collections from the Cap Prud'homme blue ice field, the Yamato Mountain blue ice field, and the South Pole Water Well at the Scott-Amundsen Station (USA), the sampled time intervals cover the last few kyr (Maurette et al., 1994), 27–33 kyr (Yada et al., 2004), and 1100–1500 AD (Taylor et al., 1998, 2000), respectively. For the most recent flux of extraterrestrial material to Earth, the MMs in central East Antarctica near the French-Italian Concordia Station – Dome C recovered from the melting and filtering of snow are considered among the most representative (Duprat et al., 2001, 2007; Gounelle et al., 2005; Dobrică et al., 2010). However, significantly older Antarctic surface sediments have also been found enriched in MMs, particularly the melted types (Hagen et al., 1989; Koeberl and Hagen, 1989; Harvey and Maurette, 1991). In the case of the TAM, sedimentary traps yield exposure ages on the order of several Ma (up to 4 Ma), linked to the high resistance of the bedrock to weathering and erosion. This is based on cosmic spherule fluences in combination with unbiased flux rate estimates, cosmogenic nuclide measurements of the exposed surface surrounding the trap, the occurrence of ∼0.8 Myr old microtektites, the presence of ∼480 kyr old ablation debris related to a large meteoritic airburst, and the paleomagnetic record of melted MMs (e.g., Folco et al., 2008, 2009; Rochette et al., 2008; Welten et al., 2008; van Ginneken et al., 2010; Suavet et al., 2011b). The TAM sedimentary traps have proven an exceptionally productive source, yielding several 1000s MMs larger than 400 μm and 100s larger than 800 μm (e.g., Rochette et al., 2008; Suavet et al., 2009).

Based on the degree of melting experienced during atmospheric passage, the distinction is generally made between melted MMs (hereafter cosmic spherules, CSs), partially melted MMs (or scoriaceous MMs), and unmelted or angular MMs (e.g., Maurette et al., 1994; Taylor et al., 1998; Genge et al., 2008). Cosmic spherules form after significant melting of micrometeoroids during atmospheric passage and subsequent cooling (Folco and Cordier, 2015). Cosmic spherules are distinct from meteorite ablation spheres, which are quenched melt droplets separated from the fusion crust of macroscopic meteorites. The latter can often be differentiated from CSs based on their lower cosmic-ray induced ^{26}Al and ^{10}Be contents and higher volatile element (mainly alkali metal) content (Raisbeck et al., 1986; Genge and Grady, 1999; van Ginneken et al., 2010).

In this work, a new sedimentary MM collection from mount Widerøefjellet in the Sør Rondane Mountains (SRM) of Dronning Maud Land in eastern Antarctica is documented, and the physicochemical characteristics of the deposits and most obvious CSs larger than 200 μm are compared to those of the TAM and other MM collections. As CSs dominate the MM influx in the size fraction larger than 50 μm, constituting a representative subpopulation for the entire MM flux (e.g., Brownlee et al., 1997;

Taylor et al., 2012; Cordier and Folco, 2014), a fraction of the largest CSs recovered from Widerøefjellet has been characterized for major ($n = 49$) and trace ($n = 44$) element concentrations, as well as for high-precision oxygen isotopic compositions ($n = 28$), after structural characterization by μCT. While the textures and chemical compositions of extraterrestrial particles are reprocessed by alteration during their terrestrial residence, this work focuses on confirming the primary nature of the MM precursor materials and refining the processes that affected these particles during atmospheric passage. While there is convincing evidence, based on elemental compositions and oxygen isotope ratio studies (e.g., Genge et al., 1997; Noguchi et al., 2002), that a large fraction of the MMs is related to carbonaceous chondrites of various clans and groups, the ratio of MMs related to ordinary as compared to carbonaceous chondrites and their distribution per size fraction, is currently based on only a limited number of analyses, especially for the larger size fractions (e.g., Steele, 1992; Kurat et al., 1994; Brownlee et al., 1997; Engrand and Maurette, 1998; Engrand et al., 2005; Gounelle et al., 2005; Genge et al., 2008; Suavet et al., 2010; Cordier et al., 2011a, 2011b; Taylor et al., 2012; Rudraswami et al., 2012, 2015a, 2015b, 2016; van Ginneken et al., 2012, 2017; Imae et al., 2013; Cordier and Folco, 2014). The ratio of carbonaceous chondrite relative to ordinary chondrite material decreases as CS diameters increase, from a factor of 10 for small particles (<500 μm in diameter) to a factor of 0.3 for larger particles, indicating that the contribution of ordinary chondrite material to the composition of the micrometeoroid complex increases with MM size, with a possible continuum between meteorites and MMs (Cordier and Folco, 2014). The present study provides an independent assessment of the flux of large (>200 μm) micrometeoroids over the last ~3 Ma and a means to evaluate the relative contributions of primitive asteroids (and comets) compared to more evolved asteroids within the interplanetary dust cloud.

2. MATERIALS AND METHODS

2.1. Sedimentary micrometeorite traps in the Sør Rondane Mountains

The Sør Rondane Mountains (SRM) within Dronning Maud Land of East Antarctica cover a surface area of approximately 2000 km^2, mainly composed of low- to high-grade metamorphic lithologies that were intruded by various plutonic rocks (e.g., Shiraishi et al., 1997). Sensitive high-resolution ion microprobe U-Pb zircon ages indicate that the last tectonothermal event in the SRM range took place 650–500 Myr ago, after which the SRM have remained geologically stable (Shiraishi et al., 2008). Ice sheet surfaces reach an elevation of about 1000 meter above sea level (masl) north of the SRM and rise to 2500 masl to the South (Suganuma et al., 2014). The region surrounding the Belgian Princess Elisabeth Antarctica (PEA) station was studied using satellite images and geological maps before the start of the 2012–2013 field campaign (Imae et al., 2015). Based on descriptions of the TAM traps

(e.g., Rochette et al., 2008; Suavet et al., 2009), erosional and eolian sediment, expected to contain significant extraterrestrial contributions, was subsequently sampled from exposed cracked and fissured surfaces at wind-exposed, high altitude (>2000 masl) granitoid summits in the western part of the SRM (Figs. 1 and 2). The current work focuses on CSs separated from a single batch of ~6.6 kg detritus collected at Widerøefjellet (~2755 masl; S72°8′41″, E23°16′41″). The main lithotype found at Widerøefjellet is a gneissose biotite-hornblende meta-tonalite, geochemically categorized as a low-K tholeiitic intrusion in volcanic arc granitoids (Kamei et al., 2013; Kojima and Shiraishi, 1986).

Limited information exists on the deglaciation history of the Widerøefjellet peak, as fully exposed or glacially abraded bedrock surfaces suitable for cosmogenic dating methods are lacking near the sampled sediment trap. However, an abraded coherent surface showing glacial striations on the granitoid Walnumfjellet in the western central part of the SRM (Fig. 1), 30 km East of Widerøefjellet at 2489 masl (S72°04′57″, E24°17′16″), indicates a ^{10}Be exposure age of 1.9 ± 0.2 Ma after correction for glacial isostatic adjustment (Suganuma et al., 2014). This exposure age is in agreement with the general glacial history for the western part of the Sør Rondane Mountains, as interpreted based on the height and degree of weathering of tills (Moriwaki et al., 1991) that were correlated to absolute ^{10}Be and ^{26}Al exposure ages (Nishiizumi et al., 1991). Prior to 4 Ma, a large part of the SRM was covered with an ice sheet that retreated progressively with some pauses prior to 1 Ma, was stagnant or re-advanced after 1 Ma, and subsequently retreated to nearly the same level as at present until ten thousand years ago (Moriwaki et al., 1991). The summit height and degree of weathering in the western part of the Sør Rondane Mountains correspond to an exposure age of ~1–3 Ma. The Walnumfjellet exposure age is taken here as a workable approximation for the deglaciation history of Widerøefjellet, until more precisely constrained. Given the annual mean air temperature of approximately −19 °C at the PEA research station (1390 masl; Pattyn et al., 2010; Gorodetskaya et al., 2013), the Widerøefjellet sediment, which lies at altitudes more than 1350 m higher than PEA, is assumed to mostly have remained below freezing point since the time of exposure. In the TAM deposits, which lie at 2600 masl (Folco et al., 2008), extraterrestrial particles have clearly been exposed to liquid water (e.g., van Ginneken et al., 2016), suggesting that melting may occur at high altitudes and ambient temperatures well below 0°C. However, contact with liquid water appears to have been less pervasive at Widerøefjellet based on the observed degree of weathering and the type of weathering minerals found on the CSs (cf. below).

2.2. Collection, sampling, and first classification

After removal of the largest rock fragments and boulders, 6.6 kg of Widerøefjellet sediment was sampled using dedicated polypropylene and wooden sampling tools, to avoid contamination by metal (Figs. 1 and 2). The sediment was gradually defrosted at temperatures only slightly
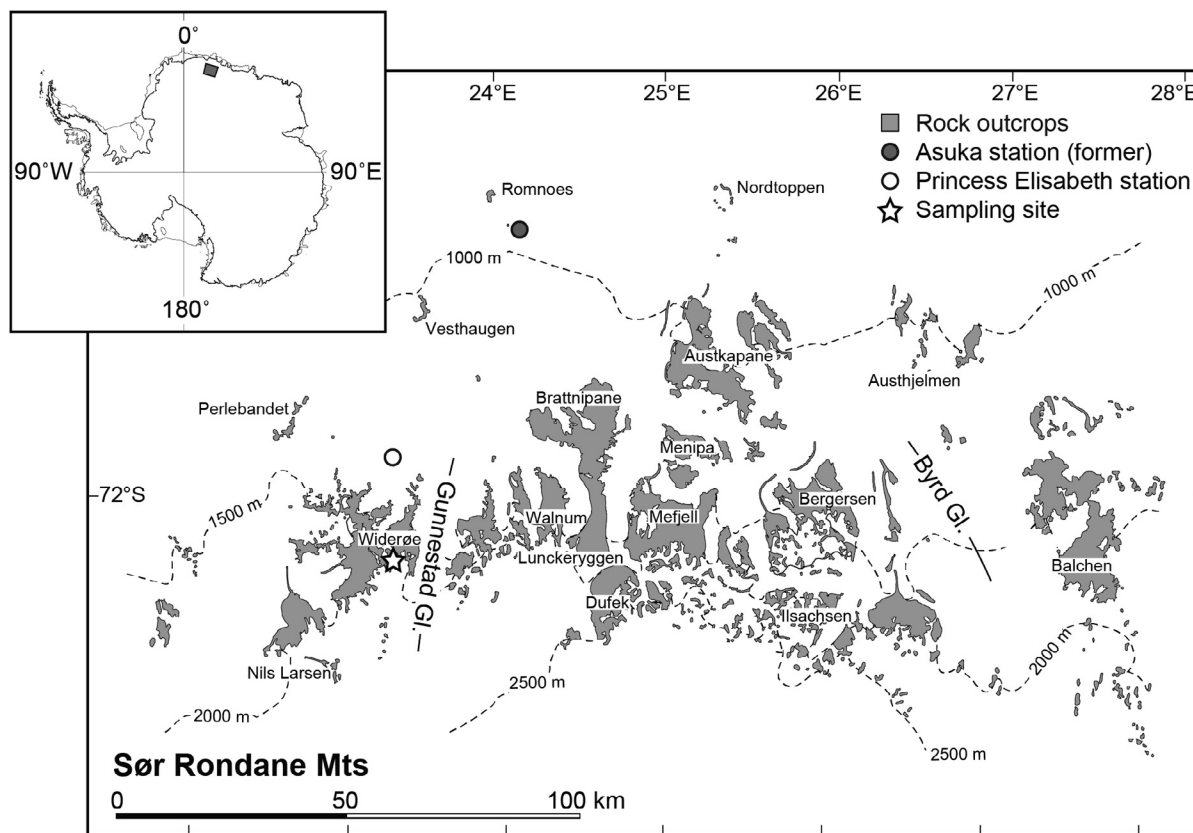
Fig. 1. Location of the Sør Rondane Mountains within Antarctica, the sites of the Princess Elisabeth (Belgium) and former Asuka (Japan) Antarctic research stations (circles), and the position of the Widerøefjellet CS accumulation site (star) relative to the Sør Rondane Mountains. Map adapted after Suganuma et al. (2014).

exceeding the freezing point at the PEA station. After sample splitting, about half of the sediment (3.2 kg) was processed by washing in milli-Q H_2O and sieving at the Vrije Universiteit Brussel (VUB, Belgium) to separate size fractions of less than 125 μm, 125–200 μm, 200–400 μm, 400–800 μm, 800–3000 μm, and more than 3000 μm, while the remaining half is kept for reference. Using optical microscopy, 2099 CSs were handpicked from the >200 μm size fractions of the Widerøefjellet deposit, with 1707 CSs extracted from the 200–400 μm, 375 CSs from the 400–800 μm, and 17 CSs from the 800–3000 μm size fractions. No extraterrestrial particles were found in the >3000 μm size fraction, while the smaller fractions and unmelted particles remain the subject of further study. For 985 randomly picked CSs, the surface textural and compositional characteristics were determined using a JEOL JSM-IT300 or field emission JEOL JSM-7000F scanning electron microscope (SEM), both equipped with energy-dispersive X-ray spectrometers (EDS), at the VUB. Cosmic spherules are traditionally divided into three compositional types following their main mineralogy: the silicate-rich (S-type) spherules, the iron-rich (I-type) spherules, and the G-type spherules, which represent an intermediate class (e.g., Blanchard et al., 1980; Taylor et al., 2000; Genge et al., 2008). Stony or silicate CSs are commonly further subdivided into four types based on quench textures, i.e., porphyritic (Po-type), cryptocrystalline (CC-type), barred olivine (BO-type) and glass or vitreous (V-type) spherules (Taylor and Brownlee, 1991; Taylor et al., 2000, 2007a; Genge et al., 2008, 2018). Recently, this classification has been expanded to include a microporphyritic type (μPo-type), as the μPo CSs appear to derive from a parent body distinct to the Po-type spherules (van Ginneken et al., 2017). Back-scattered electron images for examples of the various textural groups of silicate CSs are shown in Fig. 3. Using optical microscopy, SEM and/or μCT (cf. below), the diameters for a fraction of the extracted CSs were determined. Fig. 4 illustrates the size distribution of the Widerøefjellet CS collection and compares the size distributions of the subgroups of CSs characterized using different analytical techniques.

2.3. Micro computer-assisted X-ray tomography (μCT)

Of these 985 CSs, 45 particles in the 200–400 μm size fraction and 101 particles in the 400–800 μm size fraction were analyzed using the HECTOR (High-Energy μCT system Optimized for Research) X-ray scanner at the Centre for X-ray Tomography of Ghent University (Supplementary Fig. S1). This instrument is equipped with a 240 kV X-ray tube from X-RAY WorX and a PerkinElmer 1620 flat-panel detector of 2048 × 2048 pixels (Masschaele et al., 2013). The beam was operated at 15 kV with 90 min-
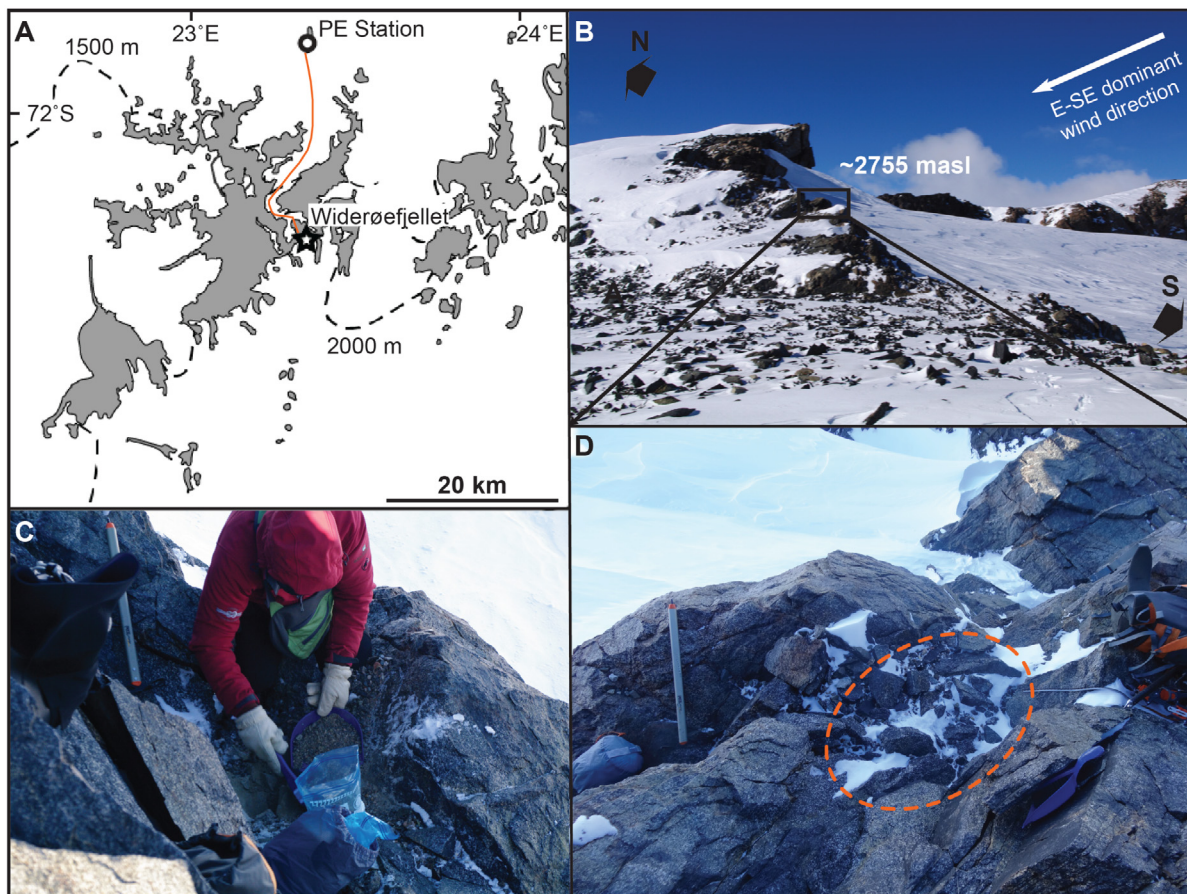
Fig. 2. Widerøefjellet CS accumulation site in the Sør Rondane Mountains. (A) Map detail of the Widerøefjellet site within the Sør Rondane Mountains region, where the CSs described in this work have been recovered. The orange line highlights the track used to reach this site, the black dashed lines represent contour lines that connect points of equal elevation (height) in meter above sea level (masl). (B) View on the Widerøefjellet summit ridge (72°09′S, 23°17′E, 2755 masl), with the box highlighting the approximate location of the MM accumulation site. Orientation and dominant wind direction are also indicated. (C-D) After removal of the largest rock fragments and boulders, the surface delineated by the orange dashed line in (D) yielded the described collection of CSs. (For interpretation of the references to colour in this figure legend, the reader is referred to the web version of this article.)

utes of exposure time per scan. Because of the size and number of MMs, packets of up to 50 particles were scanned simultaneously. Because of the variable total scanned volume, this set-up generated transmission images with a pixel size of $2 \times 2\ \mu m^2$ and $4 \times 4\ \mu m^2$ for the 400–800 μm and 200–400 μm particles, respectively. The Octopus Reconstruction software (Masschaele et al., 2007; Vlassenbroeck et al., 2007) was used to transform the acquired μCT data into a stack of 2D image slices that were consequently processed into 3D models using the open source program 3dmod Version 4.5.8. For the latter, the voxel size of the reconstructions was preferred to approximate the pixel size and ranged from $2\ \mu m \times 2\ \mu m \times 2\ \mu m$ to $4\ \mu m \times 4\ \mu m \times 4\ \mu m$. A selection of 3D μCT models is presented in Fig. 5, while examples of 2D μCT slices are shown in Supplementary Fig. S2.

2.4. Major and trace element analysis

Following the acquisition of the μCT images, 49 CSs, ranging between 439 and 916 μm, were arbitrarily selected

from the larger size fractions and mounted in epoxy resin (Polyfast™) under vacuum conditions and polished using silicon carbide paper with 1200–4000 grit (mesh) size. The exposed interiors of the spherules were subsequently polished with diamond paste in an alcohol-based suspension (particle sizes 6, 3 and 1 μm) on a synthetic cloth, and carbon-coated prior to further textural and chemical characterization using the SEM-EDS systems at VUB and electron microprobe (EMP) at the Natural History Museum (NHM) in Vienna, Austria. Quantitative wavelength-dispersive X-ray spectrometric (WDS) analyses were performed with a field emission gun electron microprobe analyser (EMPA) JEOL Hyperprobe JXA 8530F in the Central Laboratory at the NHM. Between 2 and 19 EMPA data points were gathered for relatively homogeneous particles (V- and CC-type), while more analyses were carried out for CSs with significant heterogeneity, with up to 50 points for BO- and Po-type CSs. In each CS, olivine, glass, metal and magnetite phases were examined and averaged proportional to their abundances estimated from SEM images using image processing software to obtain bulk composi-
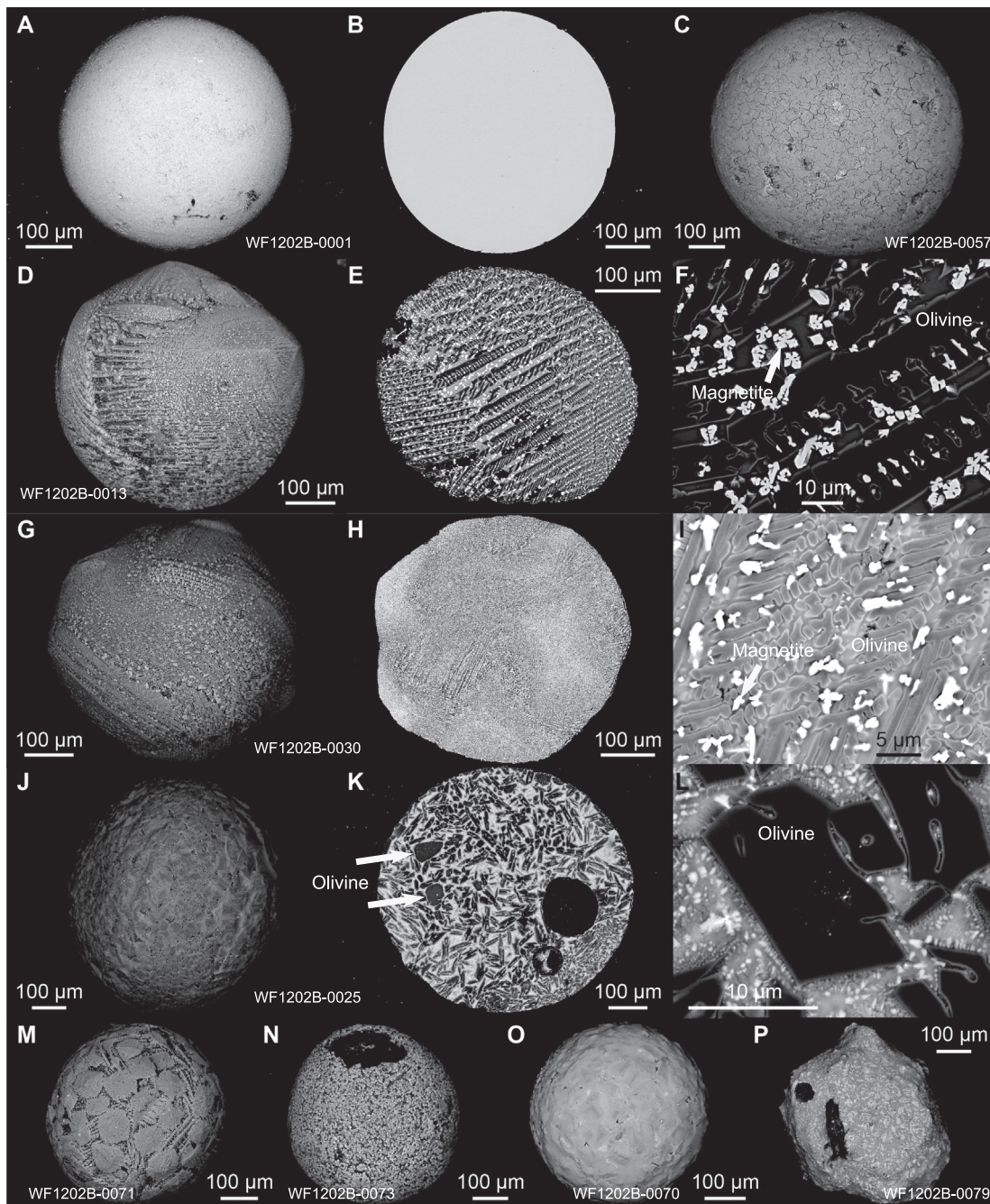
Fig. 3. Back-scattered electron images of silicate cosmic spherules characterized in this work. (A) V-type CS WF1202B-0001, displaying limited alteration. (B) Section through the same spherule. (C) V-type cosmic spherule WF1202B-0057, exhibiting a more altered, crackled surface relative to (A). (D) BO-type CS WF1202B-0013. (E) Section through the same spherule indicating local dissolution of the interstitial glass. (F) Textural detail of the same spherule showing Mg-rich olivine bars (dark grey) and magnetite crystallites (white) in Fe-rich glass (grey). (G) CC-type CS WF1202B-0030 with characteristic turtle-back (polyhedral-like) morphology. (H) A section through the same particle. (I) Textural detail of the same sectioned spherule showing olivine (grey) and magnetite crystallites (white). (J) Po-type CS WF1202B-0025, consisting mainly of olivine microphenocrysts (dark grey) in glass (grey) and magnetite (white). (K) A section through the same spherule. Note the presence of two larger, relict mineral phases, which have partially been resorbed due to atmospheric heating (indicated by arrows). (L) Textural detail of the same sectioned spherule showing microphenocryst with variable Fe-Mg contents. (M) Cosmic spherule WF1202B-0071, exhibiting a mixed BO/CC-type texture. (N) µPo-type CS WF1202B-0073. (O) Po-type "Group 4" CS WF1202B-0070. (P) Irregular CS WF1202B-0079. Particles WF1202B-0001, 0013, 0025 and 0030 were sectioned and characterized using EMPA and LA-ICP-MS, while CSs WF1202B-0057, 0070, 0071, 0073 and 0079 were analyzed as a whole for oxygen isotope ratios using LF-IRMS.
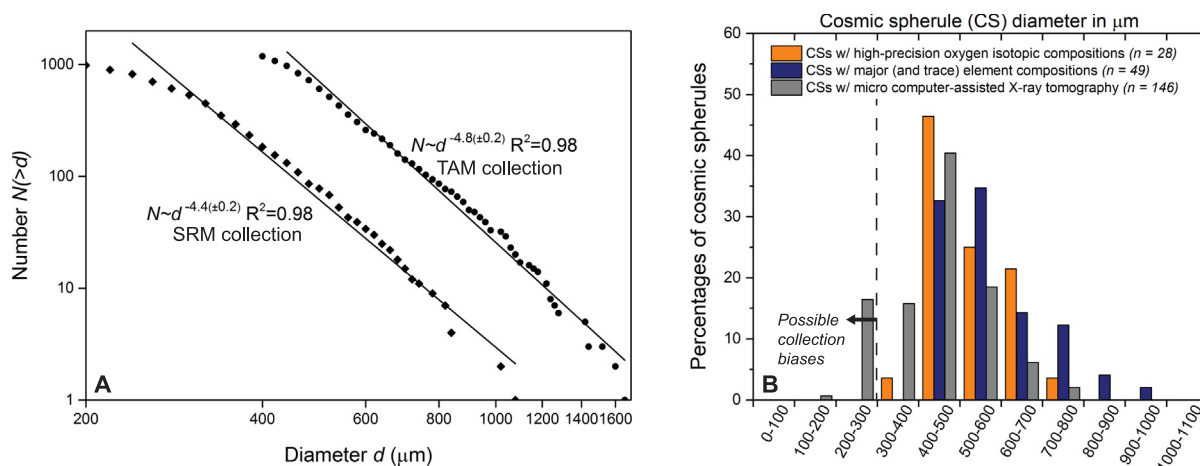
Fig. 4. (A) Cumulative size distribution for CSs from the Widerøefjellet (>200 μm size fraction, filled diamonds) and Transantarctic Mountains (>400 μm size fraction, filled circles) collections. The slopes are calculated for all samples with diameters larger than 240 μm and 440 μm, respectively, following the method described in Suavet et al. (2009). (B) Comparison of size distributions for CSs characterized for oxygen isotope ratios to those characterized for major and trace element concentrations.
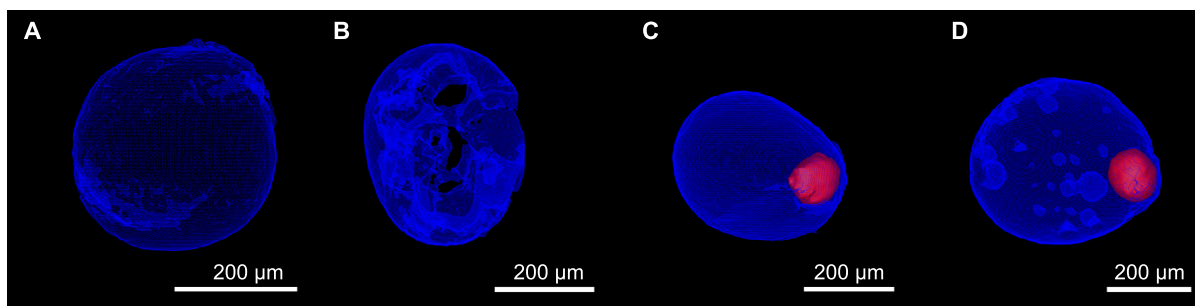

Fig. 5. Micro computer-assisted X-ray tomographic renderings for four CSs, BO-type CSs WF1202B-0002 (A), WF1202B-0042 (C) and WF1202B-0052 (D), and V-type CS WF1202B-0021 (B), highlighting the presence of metal beads (red), vesicle inclusions, or both. Additional cross-sections are provided in Supplementary Fig. S2.

tions. Note that this methodology depends on the CS section obtained and the phase contrasts within individual particles but can in part be validated through the subsequent laser ablation – inductively coupled plasma – mass spectrometry (LA-ICP-MS) analysis (cf. below). Operating conditions included an accelerating voltage of 15 kV, a beam current of 20 nA with WDS and EDS (Bruker), and a counting time of 10 s for the peak and 5 s for the background for all element K_α lines. The spot size was varied from 0.07 μm (fully focused, in the case of spatially limited phases) to 2 μm. Synthetic compounds Al_2O_3, Cr_2O_3, TiO_2, NiO, NaCl, KCl and natural minerals vanadinite $Pb_5(VO_4)_3Cl$, tephroite Mn_2SiO_4, wollastonite $CaSiO_3$, Durango apatite $Ca_5(PO_4)_5F$ and Marjalahti olivine (Mg, Fe)$_2SiO_4$ were used for calibration of Al, Cr, Ti, Ni, Na, K, V, Mn, Ca, P, Mg, Si, and Fe, respectively. The data reduction was carried out using the on-line ZAF-corrections provided by JEOL. The mean detection limits (LOD, in wt% and ppm) for the measured oxides (with standard deviation for the LOD in ppm), calculated from 50 analysis points on glass and olivine, are presented in Supplementary Table S1. The analytical precision for major elements (Si, Mg and Fe) is typically better than 1% relative

standard deviation (RSD) based on repeated measurements of calibration standards and V-type CSs, but the total uncertainty associated with the EMPA analysis, due to sample heterogeneity, is estimated to be 2–5% RSD for BO-, CC-, and Po-type CSs. For the analyzed minor and trace elements (Ti, Cr, Mn, Na, K, P, V and Ni), the total uncertainty associated with the EMP analysis is calculated to be on the order of 5–15% RSD, taking the presence of olivine and magnetite phenocrysts and changes in the composition of the interstitial glass into account. The major element data obtained using EMPA are summarized in Table 1 and Supplementary Table S1.

Selected major and trace element concentrations were determined by means of LA-ICP-MS analysis using a Teledyne Photon Machines (Bozeman, MT, USA) Analyte G2 ArF* excimer-based LA system coupled to a Thermo Scientific Element XR double-focusing sector field ICP-mass spectrometer at the Department of Chemistry of Ghent University, following the procedures outlined in Martin et al. (2013) and Van Roosbroek et al. (2015). Using a repetition rate of 30 Hz and energy density of ~8.27 J/cm^2, each CS was ablated multiple times for 15 s using a laser spot size of 50 μm. The 18 V-type CSs were each ablated

Table 1

Average major (oxide wt%) and trace (ppm) element composition with standard deviations (1 SD; italic) of textural and chemical groups of cosmic spherules determined by electron microprobe analysis (EMPA) and laser ablation-inductively coupled plasma-mass spectrometry (LA-ICP-MS), compared to the literature values compiled by Folco and Cordier (2015) for particles from other micrometeorite collections.

| Type | V normal | | V normal lit. | | BO normal[a] | | WF1202B-0013 | BO normal lit. | | CC normal | | CC normal lit. | | CAT-like | | V + BO CAT-like lit. | | High Ca-Al[b] | | WF1202B-0001 | V high Ca-Al lit. | |
| n (major/trace) | 13/13 | | 422/126 | | 11/11 | | 1/1 | 294/7 | | 9/9 | | 98/7 | | 6/6 | | 45/17 | | 3/3 | | 1/1 | 33/19 | |
	Avg.	1 SD	Avg.	1 SD	Avg.	1 SD		Avg.	1 SD	Avg.	1 SD	Avg.	1 SD	Avg.	1 SD	Avg.	1 SD	Avg.	1 SD		Avg.	1 SD
SiO_2 (wt%)	45.7	2.4	48.8	3.8	33.2	3.9	30.6	39.5	4.4	41.6	3.1	43.4	4.0	42.4	6.2	46.3	5.7	43.0	0.64	39.7	48.4	4.7
TiO_2	0.14	0.07	0.14	0.25	0.16	0.05	0.18	0.15	0.11	0.13	0.05	0.15	0.07	0.30	0.11	0.26	0.12	0.33	0.10	0.32	0.30	0.12
Cr_2O_3	0.06	0.03	0.17	0.14	0.49	0.54	1.15	0.39	0.26	0.16	0.10	0.30	0.24	<LOD	–	0.08	0.06	0.10	–	0.07	0.31	0.28
Al_2O_3	3.06	0.98	2.80	0.98	2.8	1.1	3.5	3.1	1.4	2.84	0.62	3.15	1.47	6.8	3.0	5.9	2.8	5.72	0.68	31.28	6.9	3.5
FeO^c	13.2	5.4	12.7	5.3	34.2	8.1	39.7	24.8	9.5	19.8	4.6	19.6	6.4	0.94	0.82	1.4	1.0	8.1	1.2	3.9	9.1	3.3
MnO	0.33	0.10	0.38	0.17	0.23	0.05	0.25	0.28	0.14	0.32	0.08	0.33	0.20	0.10	0.10	0.16	0.10	0.17	0.03	0.04	0.29	0.14
MgO	34.0	6.9	31.7	4.7	23.7	6.9	19.0	29.0	6.8	30.4	4.5	30.3	5.0	42.0	3.6	41.8	5.2	35.4	1.7	3.7	28.1	6.4
CaO	2.09	1.0	2.32	1.14	1.90	0.73	1.92	2.4	1.5	2.38	0.82	2.51	1.35	5.9	3.0	4.5	2.1	4.36	0.06	18.66	7.0	3.0
Na_2O	0.02	0.06	0.13	0.04	<LOD	–	<LOD	0.21	0.22	<LOD	–	0.60	0.80	0.02	0.09	0.02	0.01	0.01	0.01	0.02	0.30	0.12
K_2O	<LOD	–	0.03	0.01	<LOD	–	<LOD	0.10	0.03	<LOD	–	0.05	0.04	<LOD	–	<LOD	–	0.01	0.00	<LOD	0.06	0.01
P_2O_5	<LOD	–	0.08	0.04	0.06	0.04	0.14	0.13	0.10	<LOD	–	0.08	0.09	<LOD	–	0.18	0.09	0.05	–	<LOD	0.24	0.09
NiO	0.07	0.17	2.46	4.42	0.30	0.32	0.13	0.59	0.49	0.06	0.07	0.30	0.30	<LOD	–	0.13	0.16	0.09	0.17	0.02	0.04	0.02
Sum	98.7		101.7		97.1		96.6	100.7		97.7		100.8		98.4		100.7		97.4		97.7	100.9	
CaO + Al_2O_3 (wt%)	5.16	1.49	4.93	2.05	4.7	1.6	5.4	5.5	2.6	5.2	1.4	5.66	2.23	12.7	6.0	10.5	5.2	10.09	0.71	49.94	14.2	4.4
Fe/Mn (atomic)	40.6	12.6	40.0	20.9	156	58	155	93	49	66	28	74.7	45.2	12.7	9.1	21	25	50	15	87.0	39	20
Fe/Mg	0.24	0.12	0.48	4.72	0.92	0.42	1.17	0.51	0.27	0.39	0.17	0.39	0.15	0.01	0.01	0.02	0.01	0.13	0.02	0.58	0.20	0.10
Fe/Si	0.24	0.10	0.22	0.10	0.89	0.29	1.09	0.52	0.26	0.40	0.12	0.39	0.15	0.02	0.01	0.02	0.02	0.16	0.02	0.08	0.16	0.05
Mg/Si	1.12	0.27	0.95	0.23	1.06	0.26	0.93	1.09	0.22	1.09	0.15	1.04	0.17	1.51	0.28	1.38	0.30	1.23	0.06	0.14	0.89	0.28
Li (ppm)	0.64	0.71	0.8	–	0.37	0.50	1.72	0.6	0.4	0.74	0.56	0.9	0.6	<LOD	–	1.1	0.7	1.11	–	3.15	0.7	0.5
Sc	11.8	6.2	13.8	5.5	11	4.3	10	10.3	3.4	11.5	1.9	12.7	3.7	22.8	9.0	28	25	24	11	9	35	17
V	40	18	49	25	71	14	67	58	21	58	14	71	16	14	18	13	21	50	69	10	57	76
Cr	377	338	915	910	2091	1054	3205	2420	1460	1204	841	1650	1320	37	72	291	391	555	954	328	1132	2075
Co	31	42	32	37	270	156	370	151	113	61	27	88	52	0.21	0.15	2.6	3.6	117	202	5	19	29
Ni	381	952	568	803	2340	2761	933	3635	3675	367	436	1490	2355	1.21	0.75	422	1382	726	1539	7	134	173
Cu	0.13	0.25	NR	NR	0.08	0.06	6.62	NR	NR	0.14	0.19	NR	NR	0.9	1.6	NR	NR	0.07	0.04	0.11	NR	NR
Zn	0.47	0.24	2.3	4.4	0.39	0.13	1.84	0.70	0.35	0.68	0.73	2.27	1.48	5	11	1.3	1.5	0.45	0.13	0.65	1.8	2.9
Rb	0.2	1.1	0.12	0.17	0.01	–	2.43	0.05	0.03	<LOD	–	0.26	0.42	0.01	–	0.05	0.04	<LOD	–	0.09	0.17	0.21
Sr	10.7	4.6	11.6	7.6	13	3.2	12	10.2	2.4	15.0	4.3	12.9	6.7	29	12	26	11	21	8.8	161	33	17
Y	1.63	0.78	2.2	1.4	2.7	1.0	5.3	2.11	0.81	2.5	0.8	2.2	1.1	5.6	2.4	5.3	2.4	6.6	2.5	26.1	5.4	3.6
Zr	6.8	3.4	6.2	3.4	6.8	2.4	9.0	5.0	1.8	7.1	1.4	6.0	1.9	15.1	6.3	13	5.3	15.3	7.6	119.6	19.2	6.2
Nb	0.58	0.36	0.51	0.22	0.54	0.13	0.70	0.39	0.14	0.55	0.09	0.66	0.24	1.1	0.4	0.90	0.51	1.1	0.53	6.7	1.37	0.63
Cs	<LOD	–	0.02	0.01	0.01	0.03	0.28	<LOD	–	0.01	0.002	0.03	0.02	0.01	–	0.01	0.01	0.01	–	0.02	0.02	0.01
Ba	4.0	1.6	4.0	2.1	4.21	0.80	13.2	3.2	1.7	5.1	1.9	4.4	2.5	9.1	3.0	8.2	3.3	5.8	3.8	80.4	10.0	4.5
La	0.33	0.26	0.35	0.27	0.48	0.14	3.42	0.33	0.15	0.47	0.14	0.40	0.27	1.0	0.48	0.85	0.38	0.95	0.11	9.18	0.99	0.78
Ce	0.80	0.54	0.89	0.66	1.17	0.35	4.97	0.78	0.34	1.07	0.31	1.11	0.85	1.3	0.48	1.61	0.69	2.1	0.80	23.4	2.1	1.7
Pr	0.12	0.08	0.14	0.10	0.18	0.07	1.25	0.12	0.05	0.17	0.05	0.17	0.11	0.36	0.13	0.31	0.13	0.38	0.10	3.15	0.37	0.28
Nd	0.58	0.38	0.71	0.52	0.86	0.31	5.06	0.64	0.28	0.82	0.24	0.82	0.51	1.9	0.88	1.63	0.71	1.94	0.60	14.00	1.9	1.4

(continued on next page)

Table 1 (*continued*)

Type	V normal		V normal lit.		BO normal[a]		WF1202B-0013	BO normal lit.		CC normal		CC normal lit.		CAT-like		V + BO CAT-like lit.		High Ca-Al[b]		WF1202B-0001	V high Ca-Al lit.	
n (major/trace)	13/13		422/126		11/11		1/1	294/7		9/9		98/7		6/6		45/17		3/3		1/1	33/19	
	Avg.	1 SD	Avg.	1 SD	Avg.	1 SD		Avg.	1 SD	Avg.	1 SD	Avg.	1 SD	Avg.	1 SD	Avg.	1 SD	Avg.	1 SD		Avg.	1 SD
Sm	0.19	0.13	0.24	0.18	0.32	0.13	1.18	0.19	0.10	0.28	0.08	0.31	0.17	0.57	0.26	0.55	0.23	0.66	0.26	4.16	0.61	0.45
Eu	0.10	0.05	0.09	0.05	0.12	0.03	0.23	0.07	0.03	0.10	0.02	0.11	0.03	0.24	0.08	0.21	0.08	0.23	0.05	1.00	0.25	0.12
Gd	0.25	0.15	0.31	0.22	0.41	0.16	1.06	0.31	0.13	0.37	0.10	0.29	0.19	0.86	0.37	0.71	0.29	0.93	0.32	4.36	0.79	0.57
Tb	0.05	0.03	0.05	0.04	0.07	0.03	0.20	0.05	0.02	0.06	0.02	0.06	0.02	0.15	0.06	0.13	0.05	0.19	0.09	0.74	0.14	0.10
Dy	0.30	0.16	0.40	0.25	0.51	0.19	1.11	0.36	0.14	0.44	0.15	0.39	0.12	1.00	0.41	0.91	0.37	1.13	0.42	4.57	1.01	0.67
Ho	0.07	0.03	0.09	0.05	0.11	0.04	0.24	0.08	0.03	0.11	0.03	0.09	0.05	0.23	0.11	0.20	0.09	0.26	0.12	0.94	0.21	0.13
Er	0.21	0.11	0.25	0.15	0.34	0.12	0.71	0.25	0.11	0.32	0.08	0.27	0.14	0.73	0.33	0.60	0.26	0.77	0.30	2.91	0.64	0.4
Tm	0.03	0.02	0.04	0.02	0.05	0.02	0.11	0.03	0.01	0.05	0.01	0.05	0.02	0.11	0.04	0.09	0.05	0.11	0.04	0.38	0.10	0.05
Yb	0.23	0.14	0.29	0.15	0.34	0.12	0.61	0.24	0.10	0.32	0.08	0.29	0.14	0.70	0.29	0.62	0.23	0.79	0.38	2.40	0.64	0.32
Lu	0.04	0.02	0.04	0.02	0.06	0.02	0.11	0.04	0.02	0.05	0.01	0.05	0.02	0.10	0.05	0.10	0.05	0.12	0.05	0.34	0.10	0.05
Hf	0.21	0.13	0.19	0.10	0.22	0.08	0.30	0.15	0.05	0.23	0.04	0.19	0.06	0.46	0.21	0.39	0.14	0.50	0.29	2.76	0.51	0.20
Ta	0.03	0.03	0.03	0.01	0.03	0.01	0.03	0.02	0.01	0.024	0.005	0.04	0.01	0.06	0.03	0.06	0.03	0.06	0.03	0.26	0.08	0.04
W	0.03	0.04	NR	NR	0.21	0.14	0.18	NR	NR	0.09	0.05	NR	NR	0.01	0.01	NR	NR	0.18	0.22	0.06	NR	NR
Re[d]	0.001	0.001	NR	NR	0.01	0.02	<LOD	NR	NR	<LOD	–	NR	NR	<LOD	–	NR	NR	0.0044	0.0003	<LOD	NR	NR
Ir[d]	0.01	0.02	NR	NR	0.01	0.03	0.00	NR	NR	0.003	0.003	NR	NR	0.00	0.01	NR	NR	0.66	1.4	<LOD	NR	NR
Pt[d]	0.002	0.005	NR	NR	0.02	0.05	0.00	NR	NR	0.005	0.005	NR	NR	0.01	0.02	NR	NR	0.19	0.40	<LOD	NR	NR
Au[d]	<LOD	–	NR	NR	0.004	0.003	<LOD	NR	NR	0.002	0.003	NR	NR	0.001	–	NR	NR	0.002	–	<LOD	NR	NR
Pb	0.01	0.03	0.63	1.61	0.008	0.005	0.750	0.21	0.33	0.04	0.10	0.08	0.06	0.02	0.03	0.22	0.27	<LOD	–	<LOD	1.39	3.24
Th	0.06	0.04	0.05	0.03	0.08	0.04	0.58	0.04	0.02	0.06	0.03	0.06	0.03	0.13	0.06	0.11	0.05	0.13	0.05	1.28	0.14	0.06
U	0.00	0.01	0.01	0.00	0.01	0.02	1.00	0.01	0.01	0.01	0.02	0.02	0.02	0.02	0.05	0.01	0.01	0.00	0.10	0.14	0.01	0.00
Sc + Y + Zr + Hf (ppm)	20.5	9.6	22.4		20.9	7.2	24.9	17.6		21.3	3.7	21.1		44	18	46.4		46	58	157	60	
(La/Yb)$_N$	0.91	0.28	0.82		1.01	0.88	3.83	0.93		0.99	0.22	0.94		0.99	0.15	0.93		0.92	0.34	2.60	1.05	
Eu*	1.7	1.0	1.0		1.20	0.64	0.63	0.88		1.04	0.21	1.12		1.06	0.16	1.02		0.94	0.16	0.71	1.10	
Avg. REE$_N$	1.33	0.76	1.57		2.0	1.6	7.0	1.4		1.88	0.49	1.77		4.1	1.5	3.6		4.5	1.6	24.1	4.0	

Notes: <LOD - below limit of detection; NR - not reported or measured.

[a] Excepting WF1202B-0013.

[b] Excepting WF1202B-0001.

[c] All Fe as FeO*.

[d] Information values only.

on 2 to 4 locations, while 15 BO-type and 11 CC-type CSs were all ablated on 2–3 locations, making sure no visibly recognizable vesicles or high-density phases were targeted. The Po-type CSs were not analyzed for trace elements because of potential biases linked to individual mineral crystals.

Replicates were compared to ensure similar phases were sampled by monitoring signal intensities for the major elements Mg, Si, Ca, and Fe. Quantification was achieved through external calibration against multiple certified reference materials produced by the United States Geological Survey (USGS) and the National Institute of Standards and Technology (NIST), i.e., natural basaltic glasses USGS BCR-2G, USGS BHVO-2G, USGS BIR-1G, natural nephelinite glass NKT-1G, and synthetic glasses USGS GSC-1G, USGS GSD-1G, USGS GSE-1G, NIST SRM 610, and NIST SRM 612, using ^{29}Si as an internal standard. Based on the reference materials, the reproducibility for the reported elements is typically of the order of 5–10% RSD. The trace element data obtained for the different textural and chemical CS groups are summarized in Table 1, while the data for individual CSs are also presented in Supplementary Table S1.

2.5. High-precision oxygen isotope ratio measurements

Measurements of δ^{18}O and δ^{17}O were carried out on 28 CSs, randomly selected from the same fraction from which the CSs were prepared for major and trace element concentrations (Supplementary Fig. S1), using infrared laser-assisted (IR) fluorination isotope ratio mass spectrometry (IRMS) at the Open University in Milton Keynes, UK (Miller et al., 1999; Greenwood et al., 2017). The particles had diameters between 325 and 715 μm and were studied using SEM-EDS and μCT beforehand (Supplementary Fig. S1). Fig. 3 includes back-scattered electron images for a selection of the silicate CSs characterized for oxygen isotope ratios. Supplementary Fig. S3 indicates that the atomic Mg-Si-Fe data based on SEM-EDS for these particles fall within or close to the compositional range determined for CSs from other Antarctic, Greenland, and deep-sea collections (Taylor et al., 2000). As most of the selected CSs showed limited degrees of chemical alteration, no fracturing, and no encrustation by secondary phases based on binocular microscopy and BSE imaging (cf. below; Fig. 3; Table 2), the particles of interest were washed in acetone to remove adhesive material, but not acid-leached. Following weighing and loading, oxygen was released from the samples by reaction with BrF_5. After fluorination, the released oxygen was purified by passing the gas through two cryogenic nitrogen traps and over a bed of heated KBr. The oxygen three-isotopic composition was determined using a MAT 253 dual-inlet IRMS unit. Oxygen isotope ratios are reported in standard δ notation, where δ^{18}O is calculated as $\delta^{18}O = [(^{18}O/^{16}O)_{sample}/(^{18}O/^{16}O)_{ref} - 1] \times 1000$ (‰) and δ^{17}O using the $^{17}O/^{16}O$ ratio, relative to Vienna Standard Mean Ocean Water (V-SMOW; Table 2). To allow comparison to previously published data, Δ^{17}O, which represents the deviation from the terrestrial fractionation line (TFL), is calculated as $\delta^{17}O - 0.52 \times \delta^{18}O$

(Clayton, 1993). Accuracy and analytical precision of the method were validated by replicate analysis of international reference materials (NBS-28 quartz and UWG-2 garnet; Miller et al., 1999). Based on repeated measurement of an in-house obsidian standard, the results for subsamples with masses between 0.062 and 0.193 mg ($n = 21$; 3.69 ± 0.21‰ for δ^{17}O; 7.09 ± 0.42‰ for δ^{18}O; 0.006 ± 0.035‰ for Δ^{17}O; 2σ) show a slight systematic offset and decreased precision compared to the values obtained for larger subsamples of ~2 mg ($n = 39$, 3.81 ± 0.05‰ for δ^{17}O; 7.27 ± 0.09‰ for δ^{18}O; 0.029 ± 0.017‰ for Δ^{17}O; 2σ). This offset has been observed during previous analytical campaigns as well and may result from isotopic fractionation associated with the transfer of gas in the inlet system (e.g., Greenwood et al., 2007; Suavet et al., 2010; Cordier et al., 2011b). As the precision obtained for the small obsidian subsamples reflects the typical analytical uncertainties associated with MM analysis and the determined values for the small obsidian subsamples overlap within uncertainty with those of larger subsamples, no additional (bias) corrections were carried out. The results of the oxygen isotope measurements are summarized in Table 2, together with information on textural group, apparent diameter, mass, degree of alteration, presence of vesicles and high-density phases in the selected particles.

3. RESULTS

3.1. Textural classification and cumulative size distribution

Following SEM-EDS and μCT analysis, a selection of particles, including whole CSs and sectioned particles, were classified according to their mean bulk compositions and textural characteristics (Tables 1–3; Supplementary Fig. S1; Supplementary Table S1). The majority of CSs larger than 200 μm in the Widerøefjellet collection belong to the stony, S-type CSs (95% by number). The iron (I-type, 3%) and mixed stony-iron (G-type, 2%) types represent only small contributions to the fractions analyzed. These contributions are similar to what is observed for the TAM collections (3% I-type and 1% G-type particles; Suavet et al., 2009; Table 3). Unmelted and scoriaceous MMs have been observed but are relatively uncommon (<5%) and difficult to distinguish from mafic background mineral contributions. Of 109 randomly sampled CSs larger than 400 μm, 95% are classified as S-type (33% as V-subtype), while the G- and I-type spherules contribute 1% and 4%, respectively. A comparable distribution is observed for 228 different particles larger than 200 μm, of which 95% are classified as S-type (27% as V-subtype), with 2% and 3% contributions to the G- and I-type CSs, respectively (Table 3). The CSs studied for elemental and oxygen isotopic composition exhibit similar distributions between the textural CS groups. Of the 49 particles studied for major and trace elements, 18 (37%) are classified as V-type, 15 (31%) as BO-type, 11 (22%) as CC-type, while 5 (10%) are Po-type (Fig. 3; Table 1; Supplementary Table S1). In the case of the latter, an additional CS subtype is distinguished, the μPO-type CSs, which are mainly composed of euhedral submicron olivine crystals and are highly

Table 2

Three-oxygen isotope data for a selection of cosmic spherules from the Widerøefjellet collection, in addition to the textural group, apparent diameter and mass, degree of alteration as determined using SEM-EDS, and the presence of vesicles and high-density phases based on μCT images. A rudimentary classification summarizing to which oxygen isotopic group, as identified by Suavet et al. (2010), each particle belongs, is also included (see text for additional explanation).

Sample name	Textural group	Diameter (μm)	Mass (μg)	Weathering stage[a]	Vesicles or high-density phases (HDP)	Isotopic group	$\delta^{17}O$ ‰ VSMOW	$\delta^{18}O$‰ VSMOW	$\Delta^{17}O$‰ VSMOW
WF1202B-0053	V	465	128	Fresh (0a)	Not present	CC - Group 1	13.30	32.86	−3.79
WF1202B-0054	V	459	124	Fresh (0a)	HDP	OC - Group 3	8.19	14.68	0.56
WF1202B-0055	V	689	350	Fresh (0a)	HDP	CC - Group 1	7.15	17.91	−2.16
WF1202B-0056	BO	536	191	Fresh (0a)	Not present	OC - Group 3	8.18	14.89	0.44
WF1202B-0057	V	685	362	Moderate alteration (2a)	Vesicles	CC - Group 2	8.16	18.51	−1.46
WF1202B-0058	BO	505	166	Fresh (0a)	Not present	CC - Group 1	6.34	19.99	−4.05
WF1202B-0059	V	625	274	Fresh (0a)	Not present	^{16}O-poor - Group 4	23.96	43.54	1.32
WF1202B-0060	V	601	276	Fresh (0a)	Not present	OC - Group 3	9.04	15.83	0.81
WF1202B-0061	CC	606	253	Fresh (0a)	HDP	CC - Group 1	3.94	11.31	−1.95
WF1202B-0062	CC	522	192	Fresh (0a)	Vesicles	^{16}O-poor - Group 4	22.90	40.34	1.92
WF1202B-0063	V	622	413	Fresh (0a)	Vesicles	OC - Group 3	10.09	18.69	0.37
WF1202B-0064	BO	592	310	Fresh (0a)	Not present	CC - Group 1	2.76	12.76	−3.87
WF1202B-0065	BO	516	187	Fresh (0a)	Vesicles	^{16}O-poor - Group 4	22.59	40.03	1.77
WF1202B-0067	V	715	450	Fresh (0a)	Vesicles	OC - Group 3	9.40	17.25	0.43
WF1202B-0068	CC	492	150	Fresh (0a)	Not present	CC - Group 1	16.62	36.35	−2.28
WF1202B-0069	CC	524	143	Fresh (0a)	Not present	CC - Group 1	4.12	11.03	−1.61
WF1202B-0070	Po	439	127	Fresh (0a)	Not present	^{16}O-poor - Group 4	23.20	41.62	1.56
WF1202B-0071	BO/CC	482	187	Fresh (0a)	HDP	Ambiguous	19.08	37.18	−0.25
WF1202B-0072	CC	490	143	Fresh (0a)	Vesicles	OC - Group 3	6.42	10.51	0.96
WF1202B-0073	μPo	491	162	Fresh (0a)	Vesicles	CC - Group 1	9.42	22.77	−2.42
WF1202B-0075	V	483	144	Fresh (0a)	Not present	OC - Group 3	9.91	17.68	0.72
WF1202B-0076	BO	497	161	Fresh (0a)	Not present	CC - Group 1	14.55	32.41	−2.31
WF1202B-0077	BO	472	163	Fresh (0a)	Not present	CC - Group 1	13.05	30.65	−2.88
WF1202B-0078	CC	471	133	Fresh (0a)	Vesicles	CC - Group 1	6.18	22.04	−5.28
WF1202B-0079	Irregular	479	134	Fresh (0a)	Not present	OC - Group 3	6.43	10.95	0.73
WF1202B-0080	BO/CC	542	161	Fresh (0a)	Vesicles	CC - Group 1	11.65	28.01	−2.91
WF1202B-0101	BO	418	117	Minor alteration (1a)	Vesicles	CC - Group 1	6.25	16.25	−2.20
WF1202B-0105	V	325	45	Fresh (0a)	Not present	CC - Group 1	4.59	12.07	−1.69

Notes: Textural group: V = glassy; BO = barred olivine; CC = cryptocrystalline; Po = porphyritic; μPo = microporphyritic.
Isotopic group: CC = carbonaceous chondrite; OC = ordinary chondrite.
[a] Following classification by van Ginneken et al. (2016).

Table 3

Distribution by textural type for Widerøefjellet (WF), Frontier Mountain (FRO), Miller Butte (MIL), Larkman nunatak (LAR), Walcott Névé (WAL), South Pole Water Well (SPWW), and Indian Ocean (IO) cosmic spherules. The FRO and MIL data represent mostly magnetically separated fractions, while for the WAL data, a separation was made with heavy liquids and the light fraction was further sorted magnetically. The IO particles were separated magnetically, while the non-magnetic fractions did not yield any cosmic spherules after heavy liquid separation. Magnetic separation techniques were employed for some of the LAR samples to concentrate MMs. For the SPWW and WF collections, no bias was introduced. Data for all collections but Widerøefjellet compiled in Suavet et al. (2009), Shyam et al. (2013), and Genge et al. (2018).

Sample	Size	S-type	V-subtype	G-type	I-type	Number
WF	>400 µm	95%	33%	1%	4%	109
	>200 µm	95%	27%	2%	3%	228
FRO	>400 µm	na	na	2%	3%	331
	>200 µm	95%	15%	1%	4%	254
MIL	>400 µm	na	na	1%	3%	729
	>200 µm	na	na	na	3%	920
LAR	>60 µm	92%	19%	2%	6%	634
WAL	>100 µm	92%	10%	2%	6%	126
SPWW	>100 µm	98%	15%	1%	1%	1130
IO	>60 µm	91%	8%	3%	6%	453

Notes: na - identification of this type was not attempted or reported.

vesicular relative to normal Po-type CSs (Fig. 3; van Ginneken et al., 2017). Of the CSs characterized for oxygen isotope ratios, 10 (36%) represent V-type spherules, 7 (25%) are BO-type, 6 (21%) are CC-type, 1 (4%) belongs to the Po-type, 1 (4%) belongs to the µPo-type, while a single sub-angular, vesicular particle with dendritic and skeletal spinel crystals is classified as irregular (4%) and 2 are designated as BO/CC-type mixtures (7%; Table 2).

The diameters of the individual CSs studied here have been determined combining optical microscopy, SEM and µCT (Table 2; Supplementary Table S1). Similar to the work of Suavet et al. (2009), the particles are assumed to represent ellipsoids with equal minor and intermediate axes ($a > b = c$). As such, the diameters used in the size distribution are defined as $d_{\text{ellipsoid}} = (a \times b^2)^{1/3}$, where $d_{\text{ellipsoid}}$ represents the reported diameter of the CSs (Table 2; Supplementary Table S1). Due to the sieving process, particles may fall outside of their size fraction. As a result, a larger size fraction may contain CSs with diameters slightly below the mesh size, while conversely particles larger than the mesh size may pass into smaller mesh size sieves due to elongated shapes or mesh imperfections (e.g., Rochette et al., 2008). In Fig. 4A, the cumulative size distribution for Widerøefjellet CSs larger than 200 µm is plotted, displaying the number N of CSs larger than a certain diameter. A similar curve for a subpopulation of TAM particles larger than 400 µm, for which the unprocessed diameters were provided, is shown for comparison (Suavet et al., 2009). The size distributions for the CSs separated for chemical and oxygen isotopic analyses are plotted in Fig. 4B. Both subgroups of analyzed CSs display similar size distributions.

3.2. Metal and vesicle content

Based on the µCT scans (2D slices and 3D volumes) and sectioned SEM images (2D slices), vesicles, Fe–Ni metal beads, sulfides, and/or other inclusions with contrasting densities (including spinel group minerals) can be detected (Table 2; Fig. 5; Supplementary Table S1; Supplementary Fig. S2). Using the applied µCT system, the distinction between silicate glass and olivine cannot be made in most cases, due to the similar X-ray attenuation by these phases and the often small sizes (mostly <10 µm) of olivine crystals in BO-, CC, and Po-type CSs. Rarely, Po-type CSs are characterized by large enough olivine crystals (larger than 10 µm and up to 150 µm in size; Supplementary Fig. S2B) to be distinguished on µCT scans (e.g., WF1202B-0006, 0036, 0137, 0202). In various CSs (WF1202B-0013, 0028, 0042, 0050, 0120, 0114), µCT scans reveal internal structures in BO-type CSs that may be related to crystal orientation, although indicative lines can also be generated through interference patterns. The lower size range of vesicles and high-density phases is limited by the spatial resolution obtained for the µCT system applied. Vesicles range in diameter from <10 µm to ~200 µm, while high-density phases vary between <15–20 µm and ~100 µm (Fig. 5; Supplementary Fig. S2).

Based on the data for 146 CSs, only in part validated through 2D sections for a subset of these particles studied using SEM-EDS (Supplementary Table S1), the distinction can be made between groundmass silicate phases, high-density phases, which may include rounded Fe–Ni metal (often as metal beads), irregular sulfides, rounded to angular spinel group mineral phases, or micrometeorite-sized platinum group element nuggets (e.g., Brownlee et al., 1984; Taylor et al., 2000; Rudraswami et al., 2011; Cordier et al., 2011b), and vesicles. While most CSs with high-density phases contain only a single inclusion, multiple high-density phases, presumably FeNi metal beads, can be encountered, with up to five metal-rich inclusions within a single particle (e.g., WF1201B-0129; Supplementary Fig. S2).

Approximately 46% of the CSs between 200 and 800 µm contain no vesicles or high-density inclusions (Fig. 5; Supplementary Fig. S4A). Second most abundant (~23%) are

CSs with high-density phases but no vesicles, while CSs with vesicles, but no high-density inclusions, contribute ~22% to the studied Widerøefjellet CSs. Least abundant (~9%) are the CSs with both vesicles and high-density phases. No significant differences are observed between the studied CSs in the 200–400 μm and 400–800 μm size fractions, with the exception of a higher relative abundance of CSs with no vesicles and high-density phases in the 400–800 μm fraction relative to the 200–400 μm fraction (Supplementary Fig. S4A). When combining μCT data with textural information (Supplementary Fig. S4B), V-, BO- and Po-type CSs are dominated by particles with no vesicles or high-density phases (>57%), while only 14% of Po-type CSs fall in this category. In the case of Po-type
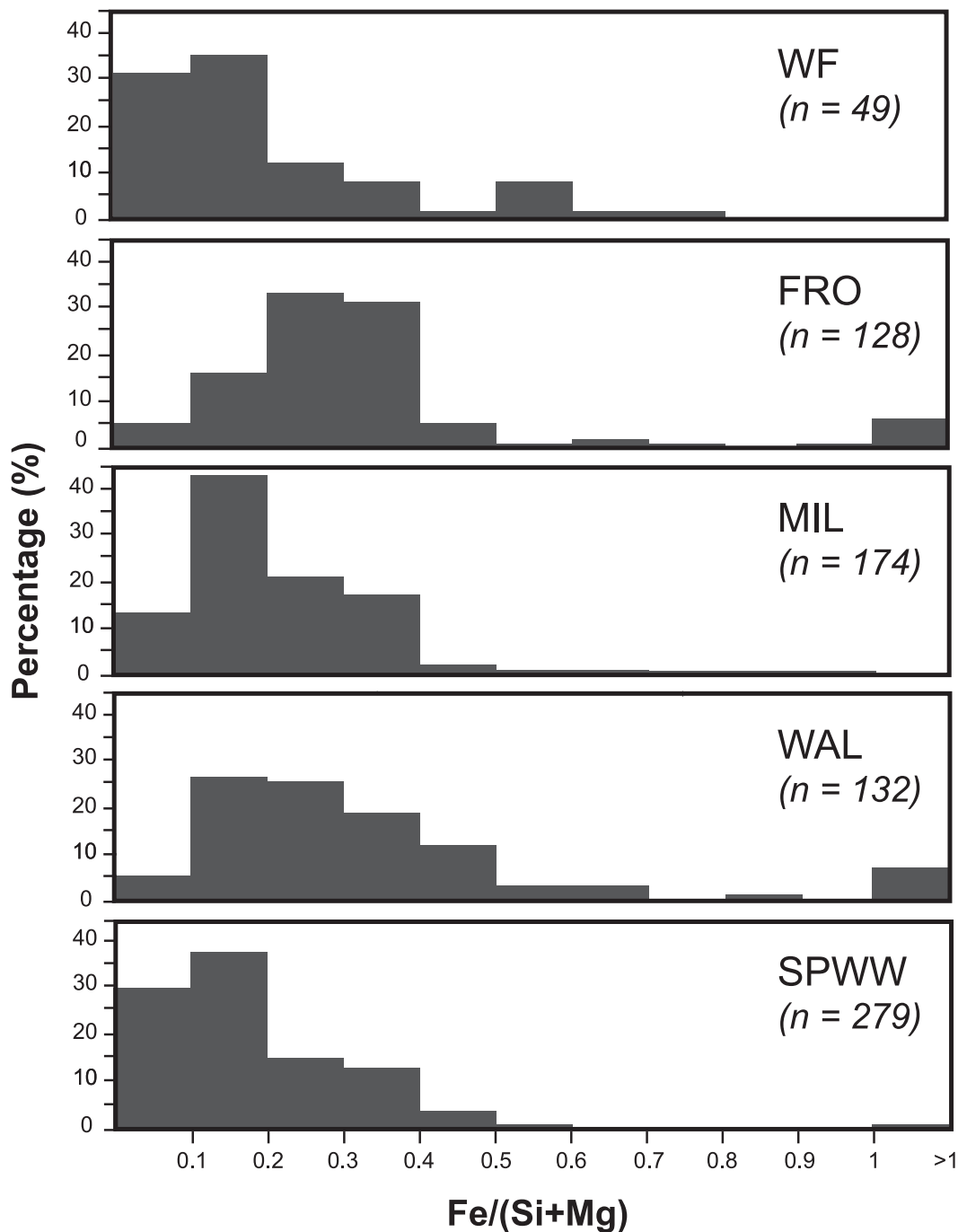
Fig. 6. Molar Fe/(Si + Mg) histograms for Widerøefjellet Mountain (WF; this work), Frontier Mountain (FRO, magnetic extract; Suavet et al., 2009), Miller Butte (MIL; Suavet et al., 2009), Walcott Névé (WAL, heavy fraction [methylene iodide, $\rho = 3300$ kg/m^3] and magnetic extract of the light fraction; Suavet et al., 2009) and South Pole Water Well (SPWW; Taylor et al., 2000) micrometeorites. All data except for Widerøefjellet extracted from Suavet et al. (2009).

CSs, particles with vesicles prevail, either with (43%) or without (43%) high-density phases. Based on these abundances, relict grain survival, vesicle formation and high-density phase segregation are linked to different degrees of atmospheric heating.

3.3. Major element composition

V-type CSs ($n = 18$) show the largest compositional variations in terms of Al, Mg, and Ca (i.e., 0.86–31.3 wt% Al_2O_3, 3.73–48.5 wt% MgO, and 0.78–18.7 wt% CaO; Table 1; Supplementary Table S1). These ranges are comparable to or larger than those reported for 187 V-type CSs from the TAM collection, with 0.06–14.1 wt% Al_2O_3, 0.85–43.0 wt% MgO, and 0.04–11.9 wt% CaO (Cordier et al., 2011b). For the CSs studied here, the largest range in SiO_2, Cr_2O_3, and FeO* (all Fe reported as FeO) concentrations is observed for BO-type spherules (Supplementary Table S1). The SiO_2 concentrations of V-type CSs display a range of 39.7–50.5 wt%, while SiO_2 contents vary between 27.4 and 42.4 wt%, 36.9 and 47.0 wt%, and 40.5–46.2 wt% for BO-type ($n = 15$), CC-type ($n = 15$), and Po-type ($n = 5$) CSs, respectively, partly overlapping (average values with 1 SD can be found in Table 1). On average, BO-type CSs contain higher bulk Fe contents than their CC-type and Po-type textured counterparts, with 28.2 wt% FeO* for BO-type versus 17.0 and 18.0 wt% FeO* for CC-type and Po-type CSs, respectively (Table 1; Supplementary Table S1). CC-type and Po-type CSs generally display comparable major element compositions, although Po-type CSs often show higher Ni contents

(1.3 wt% NiO on average) relative to other textural types (less than 0.3 wt% NiO on average for V-type, BO-type, and CC-type CSs based on EMPA data; Table 1; Supplementary Table S1). To highlight possible extraction biases, the molar Fe/(Si + Mg) ratios of the Widerøefjellet particles are compared to those of particles from various other collections (Fig. 6). On Mg-Si-Fe and K + Na-Ca-Al ternary diagrams, the SRM particles plot within the compositional ranges of CSs defined in the literature (e.g., Brownlee et al., 1997; Taylor et al., 2000; Rochette et al., 2008; Fig. 7). The extraterrestrial field is clearly distinct from literature data for Antarctic volcanic rocks and tephra. All particles studied for major and minor elements contain less than 0.35 wt% Na_2O, 0.06 wt% K_2O, and 51 wt% SiO_2, making these CSs distinct from volcanic glass shards, microtektites or meteorite ablation debris (e.g., Cordier et al., 2011b; Folco and Cordier, 2015).

All CSs characterized here exhibit relatively chondritic Mn/Mg ratios with positively correlated Fe/Mg and Fe/Mn ratios (Fig. 8A). This suggests that no particles from differentiated or basaltic precursors were sampled, as particles from differentiated parent bodies are often marked by higher Fe/Mg but similar Fe/Mn ratios relative to chondrites plotting along the horizontal lines marked "Moon" and "4Vesta/Mars" in Fig. 8A (e.g., Goodrich and Delaney, 2000; Taylor et al., 2007a; Gounelle et al., 2009; Cordier et al., 2011a,b, 2012; Cordier and Folco, 2014). Based on the atomic Fe/Si ratio and CaO and Al_2O_3 contents, chondritic CSs have previously been assigned to three distinct chemical groups (Cordier et al., 2011b): (i) the normal group containing most chondritic CSs, (ii) the
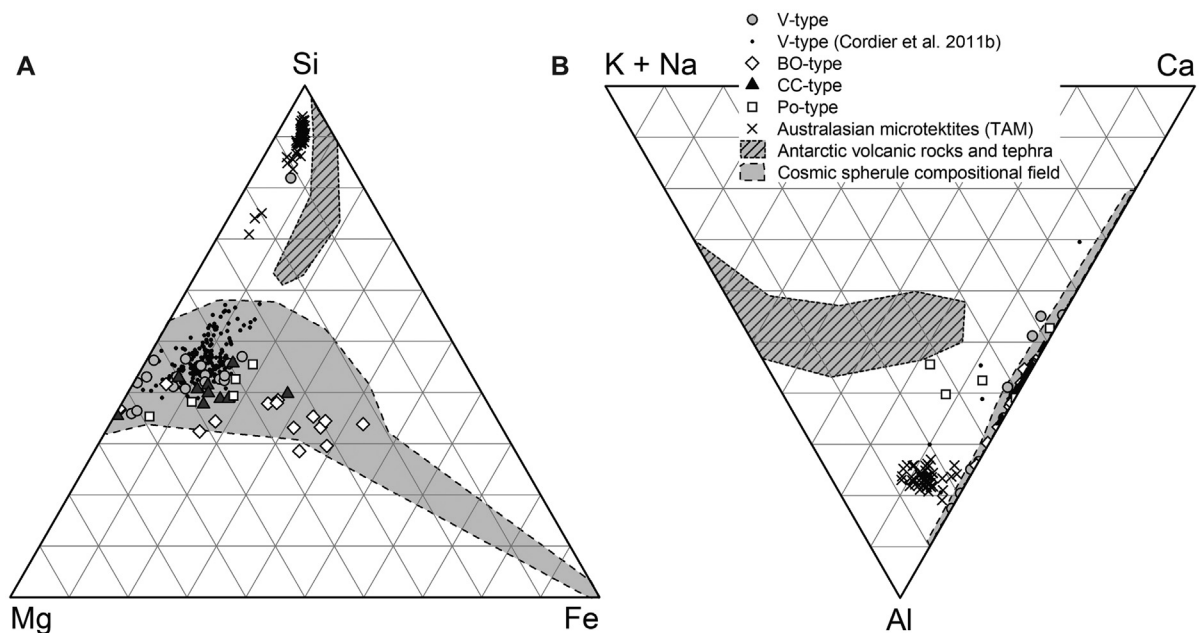

Fig. 7. Ternary atomic Mg-Si-Fe (A) and K + Na-Ca-Al (B) diagrams presenting EMPA data for a selection of CSs (V-type, BO-type, CC-type, and Po-type) recovered from the Widerøefjellet sedimentary accumulation. The elemental ranges for Antarctic volcanic rocks and tephra are based on those compiled in Rochette et al. (2008) and Suavet et al. (2009), while individual compositions of V-type CSs by Cordier et al. (2011b) are also shown. The ranges for CSs are based on other Antarctic, Greenland, and deep-sea collections (Taylor et al., 2000). Also indicated are a range of compositions of Australasian microtektites from the Transantarctic Mountains (Folco et al., 2009).
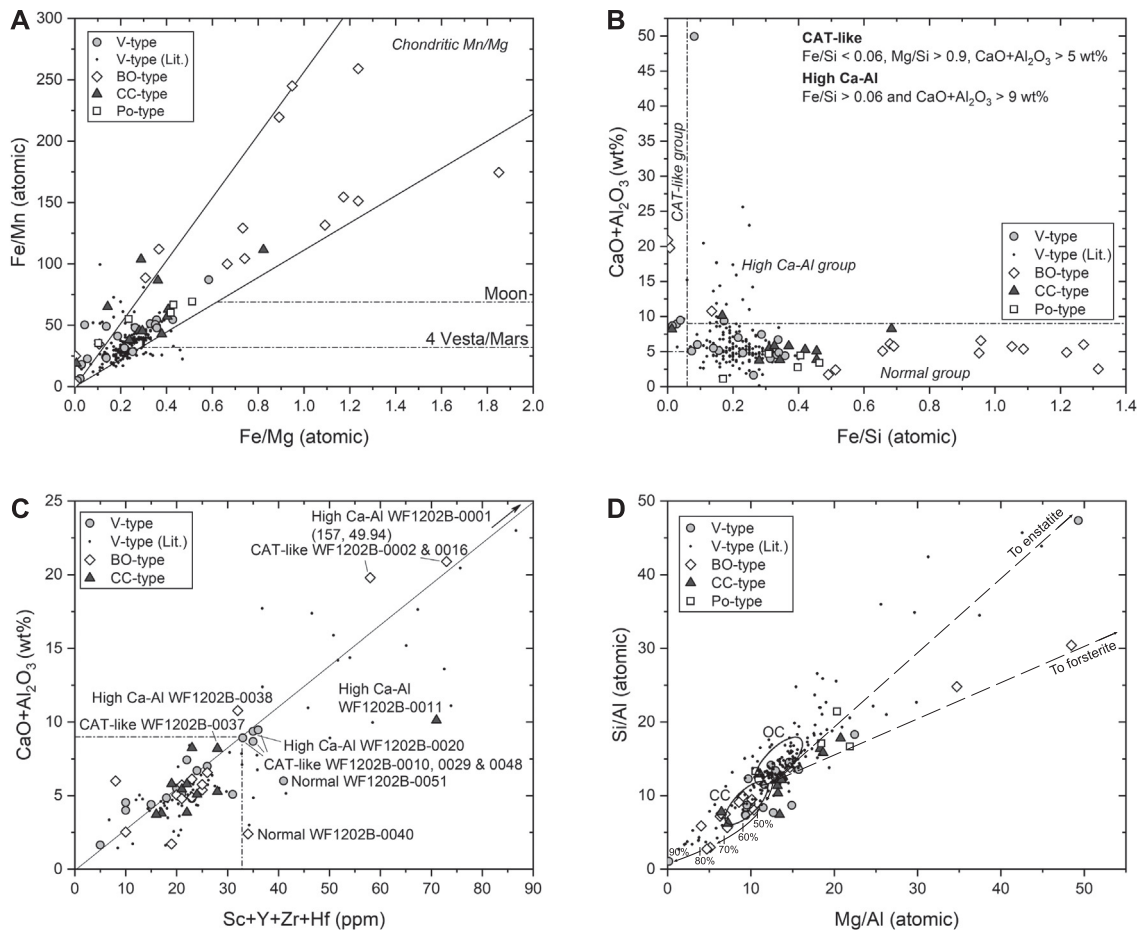
Fig. 8. Classification diagrams for silicate CSs (see details in Folco and Cordier, 2015 for A, B, and D). (A) Relationships between Fe/Mn and Fe/Mg atomic ratios. Field for chondrites and trends for achondrites are based on Goodrich and Delaney (2000). (B) CaO + Al₂O₃ content in wt.% versus Fe/Si atomic ratio. The definition for the three groups of chondritic V-type CSs are based on estimates by Taylor et al. (2000) and Cordier et al. (2011b). (C) Refractory lithophile major element content as the sum of CaO and Al₂O₃ in wt.% versus refractory lithophile trace element content, taken here as the sum of Sc, Y, Zr, and Hf in ppm. (D) Mg/Al versus Si/Al atomic ratios. An evaporation trajectory is drawn from the Ivuna-type (CI) carbonaceous chondrite precursor (fields from Jarosewich, 1990). Regardless of the starting composition, evaporation trajectories for carbonaceous and ordinary chondritic compositions converge after ~30% of the material has evaporated (Alexander et al., 2002). The arrows labeled "enstatite" and "forsterite" show the mineralogical control of precursor material on the bulk CS composition (CC = carbonaceous chondrite field; OC = ordinary chondrite field). V-type (Lit.) from Cordier et al. (2011b).

Ca-Al-Ti-rich (CAT-like) group with $Fe/Si < 0.06$, Mg/ $Si > 0.9$ (at%) and $CaO + Al_2O_3 > 5$ wt%, and (iii) the high Ca-Al group with $Fe/Si > 0.06$ (at%) and $CaO + Al_2O_3 > 9$ wt% (Fig. 8B). This classification extends and refines the chemical characteristics (low Fe/Si and high Mg/Si ratios) of the previously identified "CAT" group, defined by Taylor et al. (2000) and Alexander et al. (2002). Applying the criteria defined above, 6 (12%) of the CSs studied here belong to the CAT-like group (V-type WF1202B-0010, 0029 and 0048, BO-type WF1202B-0002 and 0016, CC-type WF1202B-0037; Supplementary Table S1), while 4 of these 49 CSs (8%) can be classified as high Ca-Al spherules (V-type WF1202B-0001 and 0020, CC-type WF1202B-0011, BO-type WF1202B-0038). It should be noted that high Ca-Al particle WF1202B-0038 is also characterized by a high TiO₂ content of 0.36 wt%, perhaps rendering this classification scheme incomplete. Both CAT-like and high Ca-Al particles are thus represented among all textural

CS groups, excepting Po-type CSs. While the abundance of high Ca-Al particles is comparable to that observed in the V-type CS population of the TAM collection (10%), CAT-like particles are significantly less abundant in the V-type subpopulation of the TAM collection (~2%; Cordier et al., 2011b). As the V-type CSs in the latter work are comparable in size (220–850 μm) to the Widerøefjellet particles studied here, the higher abundance of CAT-like particles here indicates a higher proportion of such CSs among the non-glassy textural groups.

3.4. Trace element composition

The CSs studied exhibit a large diversity in REE contents and patterns (Figs. 8C, 9, 10, 11), which are difficult to relate to any particular chemical or textural group. On average, the V-type, BO-type, and CC-type textural groups show fully chondritic REE ratios and superchondritic con-
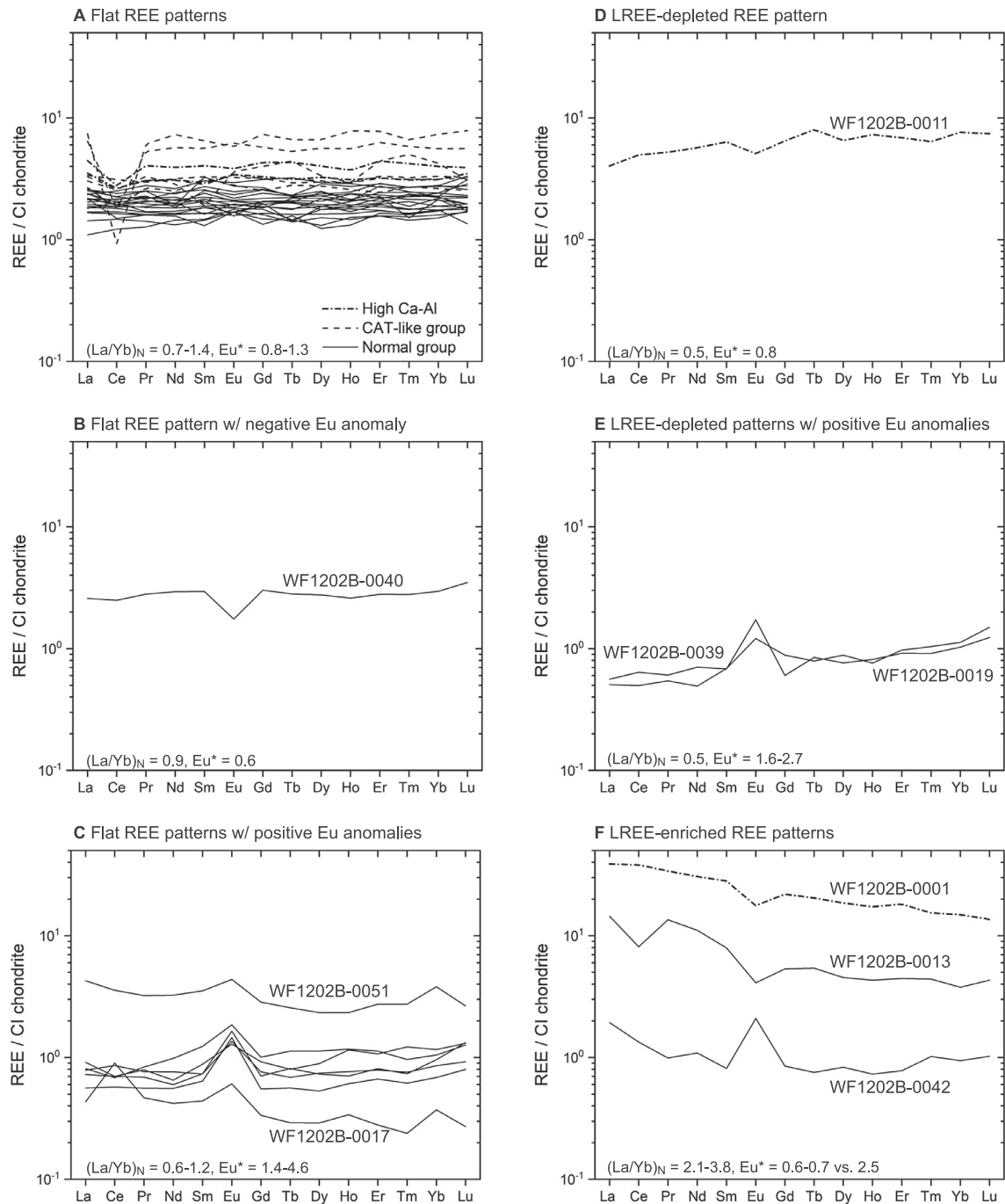
Fig. 9. The categories of REE patterns observed among CSs of Widerøefjellet. Normalization to CI chondrite composition (McDonough and Sun, 1995). While five of the patterns correspond to those identified by Cordier et al. (2011b), the LREE-enriched patterns in (F) differ slightly from the previously identified ''U-shaped'' pattern.

centrations (La/Yb_N of 1.0, 1.2, and 0.95, Eu* of 1.6, 1.1, and 1.0, average REE_N of 3.0, 3.0, and 2.3 for V-, BO-, and CC-type, respectively; Table 1). CC-type CSs exhibit the least variable REE patterns, while BO-type CSs display the most pronounced Ce depletions, with a mean Ce* of 0.84 (with $Ce^* = Ce_N/\sqrt{[La_N * Nd_N]}$), compared to mean Ce* of 1.0 and 0.92 for V- and CC-type CSs, respectively. These Ce anomalies in BO-type spherules are mostly inher-ited from CAT-like and high Ca-Al group CSs (mean Ce* of ~0.36 for CAT-like WF1202B-0002 and 0016, and high Ca-Al WF1202B-0038; Fig. 11). Based on the fractionation observed between light, medium, and heavy REEs, in com-bination with the presence or absence of Ce and Eu anoma-lies (defined based on $Eu^* = Eu_N/\sqrt{[Sm_N * Gd_N]}$), seven different REE patterns can be recognized among the CSs characterized in this work ($n = 44$; Fig. 9A–F; Supplemen-
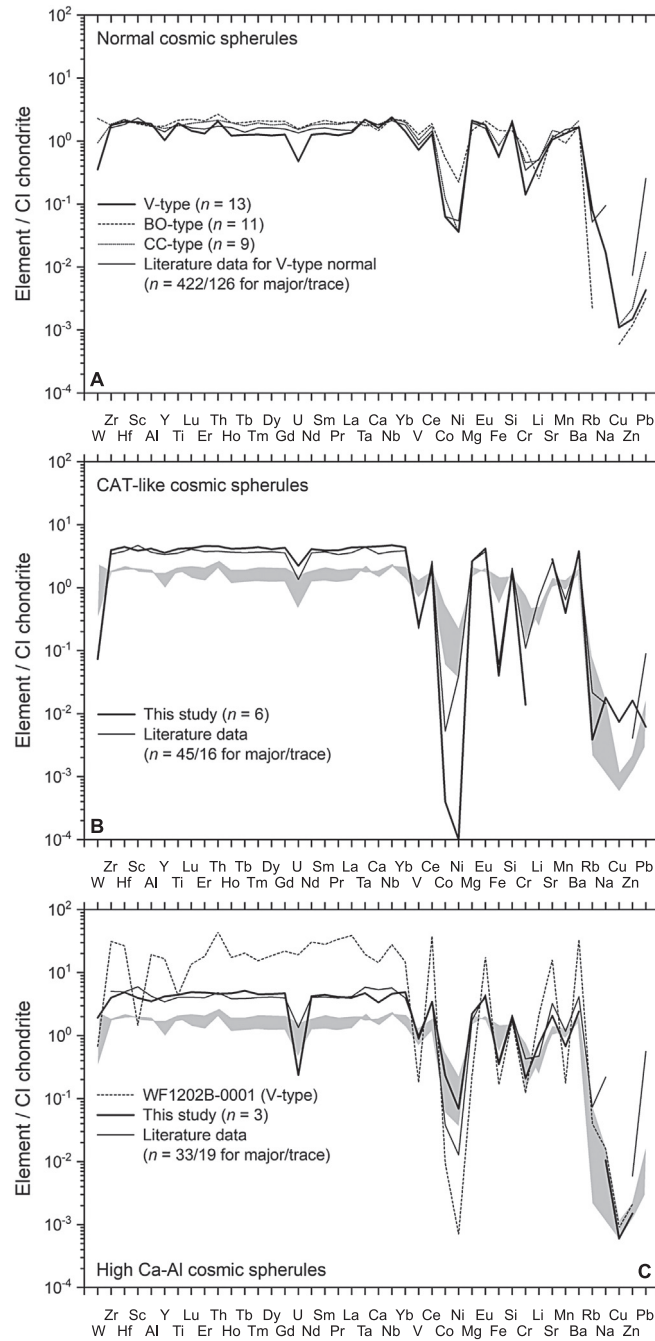
Fig. 10. Comparison of major and trace element compositions for the normal V-type, BO-type, and CC-type, CAT-like, and high Ca-Al CS groups recognized among the Widerøefjellet particles and in literature (Folco and Cordier, 2015; Table 1). Concentrations are normalized to CI chondrites (McDonough and Sun, 1995). Elements are ordered according to increasing volatility (i.e., 50% decreasing condensation T_C at 10^{-4} bar; Lodders, 2003) from left to right.

tary Table S1): (A) CSs with flat patterns (La/Yb$_N$ = 0.7–1.4; Eu* = 0.8–1.3; n = 29). These CSs make up 82% of the CC-type, 75% of the BO-type, and 50% of the V-type spherules. Most of these CSs exhibit fully chondritic REE patterns (Ce* ∼0.7–1.2), while two CAT-like BO-type spherules show strong Ce depletions with Ce* of less than 0.3 (WF1202B-0002 and 0016). (B) One BO-type CS

(WF1202B-0040) shows a flat REE pattern with a negative Eu anomaly (La/Yb$_N$ = 0.9; Eu* = 0.6). (C) Eight CSs, mostly V-type (75%), are characterized by a flat REE pattern with positive Eu anomaly (La/Yb$_N$ = 0.6–1.2; Eu* = 1.4–4.6). One of the V-type CSs of this group (WF1202B-0017) exhibits a positive Ce anomaly (Ce* of 2.0 compared to 0.8–1.1 for the other CSs with this type

of pattern). (D) One CC-type CS (WF1202B-0011) exhibits a LREE-depleted pattern (La/Yb$_N$ = 0.5; Eu* = 0.8). (E) Two V-type spherules (WF1202B-0019 and 0039) show LREE-depleted patterns with positive Eu anomalies (La/Yb$_N$ = 0.5; Eu* = 1.6–2.7). (F) One V-type (WF1202B-0001) and one BO-type (WF1202B-0013) CS are characterized by LREE-enriched patterns with negative Eu anoma-

lies (La/Yb$_N$ = 2.6–3.8; Eu* = 0.6–0.7). The BO-type CS also shows a slight negative Ce anomaly (Ce* of 0.6). (G) BO-type CS WF1202B-0042 exhibits a LREE-enriched pattern with a positive Eu anomaly (La/Yb$_N$ = 2.1; Eu* = 2.5).

The chemical groups of CSs also vary in their trace element compositions (Table 1; Figs. 8–11). The mean
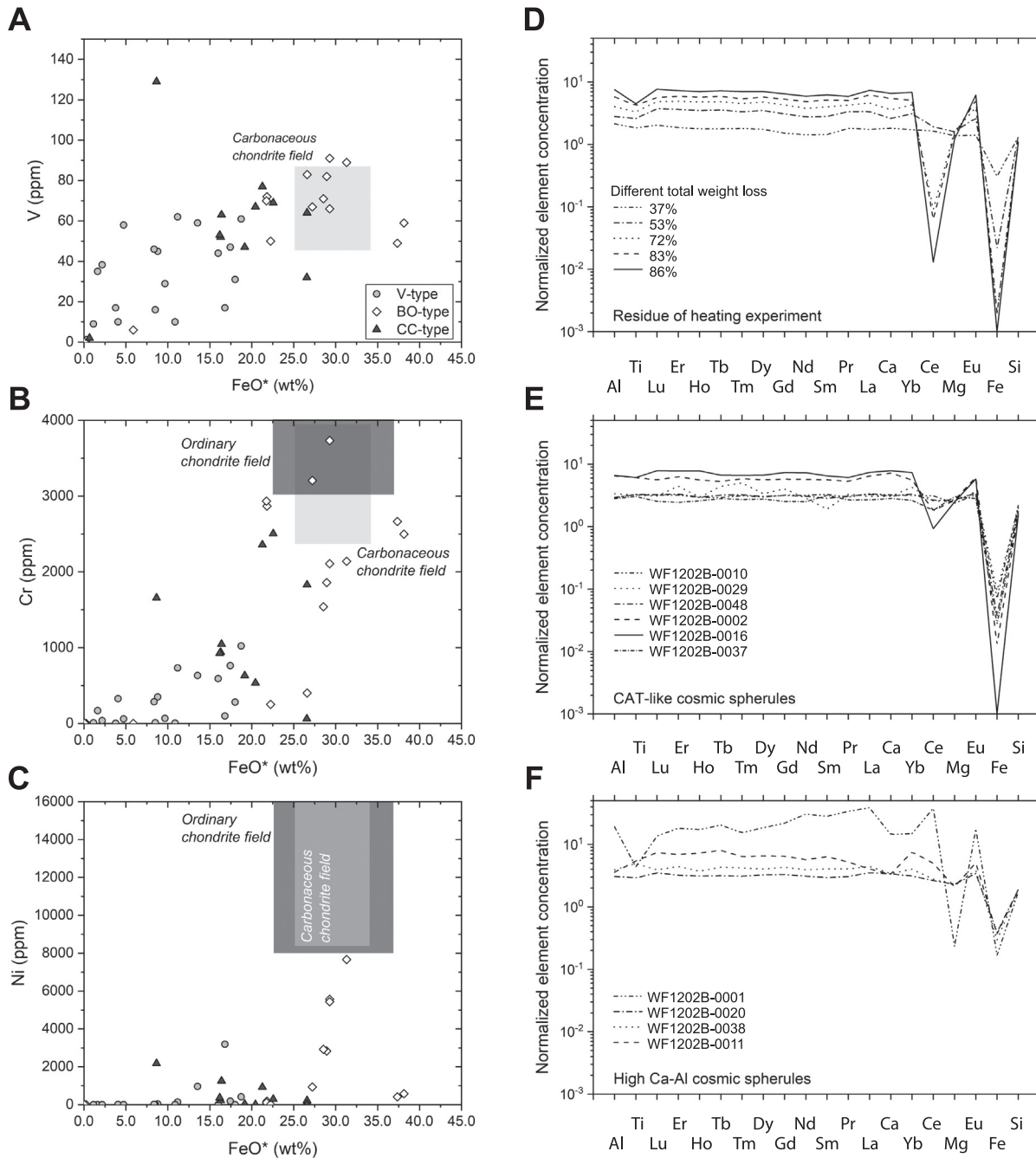
Fig. 11. (A–C) Binary plots of (partially) siderophile elements V, Cr, and Ni versus FeO*, as determined by LA-ICP-MS in this work. Fields for ordinary chondrites and carbonaceous chondrites (2 SD of the mean) based on Cr, Ni, and FeO* data from Jarosewich (1990) and V data from Friedrich et al. (2002). (D–F) Comparison of average major and trace refractory element concentrations in residues of heating experiments with varying total weight loss in % (Wang et al., 2001) with the CAT-like and high Ca-Al CS patterns determined in this work. The compositions of the CSs are normalized to CI chondrite (McDonough and Sun, 1995), while those of the residues are normalized to the starting solar composition (Wang et al., 2001).

values for the chemical CS groups determined in this work indicate excellent correspondence to the group averages compiled in literature based on particles from different MM collections (Table 1; Fig. 10; Folco and Cordier, 2015). Relative to CI chondrites, the normal group exhibits an enrichment in refractory elements (50% condensation temperatures above 1360 K), excluding siderophile W and chalcophile V as well as redox-sensitive Th and U, to values of ∼1.5–2.3, with a mean REE_N equal to 1.9 ± 1.2 times CI (1 SD; n = 34; Fig. 10). On average, the siderophile elements W, Ni, and Co and chalcophile elements V and Cr are depleted by approximately one order of magnitude relative to refractory elements, although particular CSs show element depletions by four orders of magnitude. The flat refractory element patterns of these CSs are occasionally also interrupted by both positive and negative anomalies in Sc, Y, Th, U, Ta, Nb, and Ce, but on average most of these elements, except for Th, U, and Ce, are not depleted relative to chondrites and exhibit chondritic ratios (Fig. 10). Mean positive Th and U anomalies were previously not observed for V-type spherules (Cordier et al., 2011b), but can be present in CSs as exemplified by BO-type CS WF1202B-0013, for this reason this particle is not included in the BO-type average in Fig. 10A. The depletion in volatile Rb, Na, Cu, Zn, and Pb may not be linked directly to element condensation temperatures, as Pb is present at higher concentrations than all other volatile elements. Alternatively, the relative Pb enrichment may be due to contamination during LA-ICP-MS analysis.

The CAT-like CSs are distinct from the normal group by a higher enrichment in refractory elements (∼2.1–4.9 × CI), with a mean REE_N equal to 4.1 ± 1.5 times CI (1 SD; n = 6; Fig. 10), and a stronger mean depletion in siderophile elements W, Co and Ni (by ∼1–4 orders of magnitude). Chalcophile Cr, V, and Mn are depleted to 0.2–0.02 times CI on average (Fig. 10). On average, CAT-like CSs exhibit a negative U anomaly comparable to that of the normal chondritic CS group, although individual spherules can be U-enriched, as seen for BO-type CS WF1202B-0016 (Supplementary Table S1). The depletion in volatile Rb, Na, Cu, Zn, and Pb is not as pronounced as for the normal chondritic CSs, mostly as the result of V-type CS WF1202B-0029 that shows a less volatile element-depleted signature.

The high Ca-Al spherules show the highest enrichment in refractory elements of all groups (∼2.4–5.2 × CI), with a mean REE_N equal to 4.5 ± 1.6 times CI (1 SD; n = 3; Fig. 10). This mean value excludes V-type CS WF1202B-0001 characterized by an even higher REE enrichment factor of ∼24 relative to CI chondrites (Supplementary Table S1). All high Ca-Al spherules exhibit a negative U anomaly, although limited in WF1202B-0001. The relative depletions in siderophile W, Co, and Ni and chalcophile Cr, V, and Mn for the average high Ca-Al group are intermediate between those of the normal and CAT-like groups (Table 1; Fig. 10). The depletion in volatile Rb, Na, Cu, Zn, and Pb is similar to or larger than that observed for the normal CSs.

3.5. Oxygen isotope ratios

The $\delta^{18}O$, $\delta^{17}O$ and $\Delta^{17}O$ values for 28 CSs are reported in Table 2. These CSs, with diameters ranging from 325 to 715 μm and masses between 45 and 450 μg (see Section 2.5; Supplementary Fig. S5), were randomly selected from the Widerøefjellet collection and analyzed for their three-oxygen isotopic compositions. Based on BSE images of whole particles, these CSs have been assigned to the BO-type (n = 7, ∼25%), Po-type (n = 2, ∼7%), V-type (n = 10, ∼36%), and CC-type (n = 6, ∼21%) textural groups (Genge et al., 2008; Table 2). One CS has an irregular appearance, while 2 other particles represent BO/CC-type mixtures (Fig. 3; Table 2). This distribution by types is similar to that of unbiased collections (e.g., Taylor et al., 2000; Cordier and Folco, 2014), and consistent with the 49 Widerøefjellet CSs characterized for major and trace element concentrations (Supplementary Table S1). In Fig. 12, the $\Delta^{17}O$ data versus $\delta^{18}O$ of the CSs are shown relative to the TFL and the oxygen isotopic compositions of various chondrite groups (Clayton et al., 1991; Clayton and Mayeda, 1999; Newton et al., 2000). Fig. 12A compares the data from this work to high-precision oxygen isotopic data determined for Antarctic CSs by IRMS available from literature (Cordier et al., 2011a, 2012; Suavet et al., 2010, 2011a), while Fig. 12B links the acquired data to the values determined for eighteen >500 μm diameter CSs from the Atacama Desert in Chile (van Ginneken et al., 2017) and includes textural information.

The oxygen isotopic compositions of the CSs characterized here can be compared to the four groups previously defined qualitatively by Suavet et al. (2010) (Fig. 12A). A fifth group is often added to these four to accommodate for HED-like materials (e.g., Cordier and Folco, 2014 and references therein). Below the TFL, 3 of 10 V-type, 5 of 7 BO-type, 1 of 2 Po-type, 4 of 6 CC-type CSs, and 1 mixed BO/CC-type CS exhibit isotopic compositions that fall within or close to the *Group 1* field, defined to exhibit $\Delta^{17}O$ values below −2.2‰ and $\delta^{18}O$ values of 8 to 32‰ (Suavet et al., 2010). A single V-type CS WF 1202B-0057 has an isotopic composition that can be considered to be part of *Group 2,* previously constrained to range from −0.2 to −1.5‰ for $\Delta^{17}O$ with $\delta^{18}O$ of ∼25‰ (Suavet et al., 2010). One V-type (WF1202B-0105) and 2 CC-type CSs (WF1202B-0061 and 0069) fall in between *Group 1* and *Group 2* and cluster closer to meteoritic values, with $\Delta^{17}O$ between −2.0 and −1.6‰ and $\delta^{18}O$ around 12‰. Mixed BO/CC-type CS WF1202B-0071 with a $\Delta^{17}O$ of −0.25 and $\delta^{18}O$ of 37.2‰ remains ambiguous and cannot be assigned to either *Group 1* or *Group 2*, or any particular chondrite group. Above the TFL, five V-type, 1 BO-type, 1 CC-type CS, as well as 1 CS with an irregular texture have isotopic compositions that fall within or close to the *Group 3* field, defined to display $\Delta^{17}O$ values between 0.1 and 1.0‰ and $\delta^{18}O$ values of ∼15‰; Suavet et al., 2010). One CS of each main textural group (V-, BO-, CC-, and Po-type) is characterized by an isotopic composition close to that of the ^{16}O-poor *Group 4*, with $\Delta^{17}O$ of ∼2‰ and $\delta^{18}O$ equal or larger than 40‰ (Suavet et al., 2010).
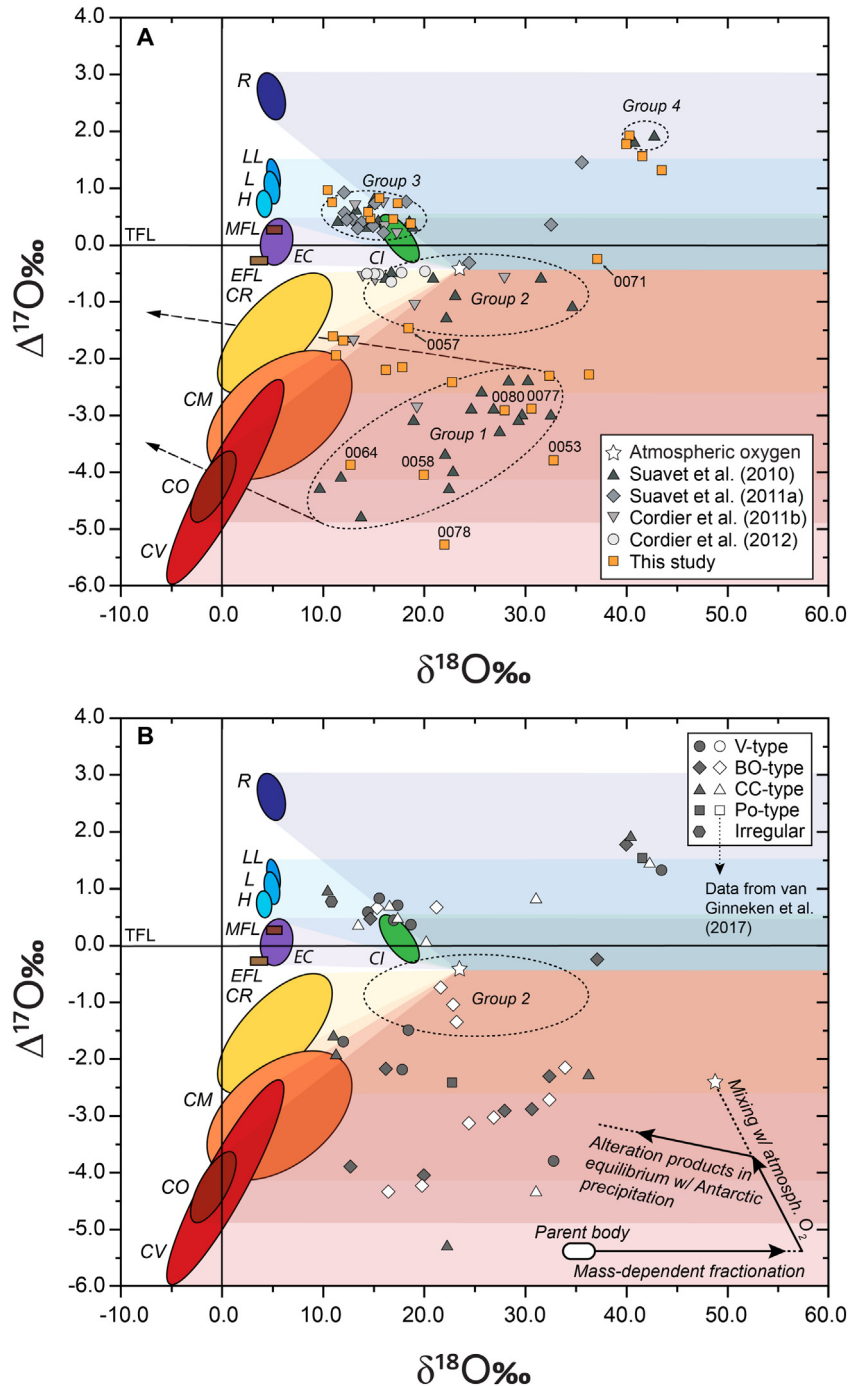
Fig. 12. $\delta^{18}O$ (horizontal) versus $\Delta^{17}O$ (vertical) in ‰ for the individual CSs from Widerøefjellet measured in this work compared to literature IRMS data for (A) Antarctic CSs (Suavet et al. 2010, 2011a; Cordier et al., 2011a, 2012) and (B) CSs from the Atacama Desert in Chile (open symbols; van Ginneken et al., 2017). The data from this work are shown by orange squares in (A) and filled dark grey symbols in (B). The solid line labeled TFL represents the terrestrial fractionation line ($\approx \delta^{17}O = 0.52 \times \delta^{18}O$), while the average isotopic composition of oxygen around the transition from the stratosphere to the mesosphere ($\delta^{18}O \approx 23.5$‰ and $\delta^{17}O \approx 11.8$‰; Thiemens et al., 1995) is represented by a star. Plot (A) is adapted after Suavet et al. (2010) and Cordier and Folco (2014), with colored domains representing potential parent bodies (Clayton et al., 1991; Schulze et al., 1994; Clayton and Mayeda, 1999; Newton et al., 2000) and shaded areas indicating the range of possible values for a micrometeorite derived from a particular parent body. Mass fractionation lines for asteroid 4 Vesta (EFL, $\Delta^{17}O = -0.242 \pm 0.016$‰; Scott et al., 2009) and Mars (MFL, $\Delta^{17}O = 0.301 \pm 0.013$‰; Franchi et al., 1999) are also shown. The outlines of the 4 groups originally identified by Suavet et al. (2010) are represented using dotted lines, while the dashed arrows reflect the direction of possible shifts due to the formation of alteration products in equilibrium with Antarctic precipitation. Individual CSs are highlighted using their number designation only, as these all share the common prefix "WF1202B-". Plot (B) includes textural information on the individual particles and illustrates the three possible effects by which the bulk O isotopic composition of a CS can be changed starting from chondritic parent body values. Analytical uncertainties for IRMS measurements are ± 0.42‰ for $\delta^{18}O$ and ± 0.04‰ for $\Delta^{17}O$ (2σ). As ion microprobe data are generally associated with larger uncertainties (± 1‰ for $\delta^{18}O$ and ± 0.7 for $\Delta^{17}O$) and show much larger variability because of the characterization of individual mineral phases, such literature data are not included here.

4. DISCUSSION

4.1. Accumulation mechanism for Widerøefjellet

Natural concentration and alteration processes (e.g., wind sorting, interaction with fluids) and sampling methods (e.g., sieving, magnetic separation, hand-picking) may introduce biases in the physicochemical properties of a MM collection. The Concordia collection, recovered by melting large volumes of Antarctic snow, is considered one of the least biased collections based on the high abundance of fragile fine-grained fluffy and ultracarbonaceous particles as well as the occurrence of sulfides prone to weathering (e.g., Nakamura et al., 1999; Duprat et al., 2007, 2010; Dobrică et al., 2012; Genge et al., 2018). However, CSs are not described for this collection (Dobrică et al., 2010), preventing a direct comparison with collections recovered from deposits with longer accumulation ranges, such as blue ice-derived collections and sedimentary accumulations. As an example, fine- and coarse-grained unmelted particles are significantly less abundant in the SPWW (Taylor et al., 1998, 2000, 2007b), Cap Prud'homme (Kurat et al., 1994; Genge et al., 1997), Larkman Nunatak (Genge et al., 2018), or TAM (Rochette et al., 2008) collections relative to the Concordia collection (Dobrică et al., 2010), indicating terrestrial reprocessing or collection and operator biases.

Despite different particle size distributions for various collections, the abundance of CS types may also provide some insight regarding potential collection biases. For example, magnetite and wüstite-dominated I-type CSs, relatively resistant to weathering, represent 1% of all CSs larger than 100 μm in the SPWW collection, generally considered a relatively unbiased MM collection (Table 3; Taylor et al., 2000, 2007a; Rochette et al., 2008; Genge et al., 2018). Slightly higher abundances of I-type particles (3–4% of all CSs > 200 μm) have been observed in the TAM collection, while even higher values in the Larkman (6% of all CSs > 60 μm), Walcott Névé (6% of all CSs > 100 μm), and Indian Ocean (6% of all CSs > 60 μm) collections likely indicate higher weathering degrees, taking into account the respective collection size ranges (Table 3). Mid-Pacific abyssal clays up to 500 kyr old form an extreme example, with I-type particles constituting 25 to 50% of the extracted CSs, based on 700 particles of 0.1–1 mm where the variation depends on the core samples and magnetic extraction procedures employed (Blanchard et al., 1980). If no metal-bearing I-type spherules were lost, the comparable degree of I-type enrichment in the Widerøefjellet and TAM collections relative to the SPWW collection may indicate a significant loss of S-type particles due to weathering or wind transport, although potential biases linked to particle size distributions remain difficult to evaluate.

Particle losses may be detected by studying the cumulative size distribution of the Widerøefjellet collection relative to those of other collections (Fig. 4A). To account for the diversity of procedures that exist to construct cumulative size distributions (e.g., Taylor et al., 2000, 2007b; Suavet et al., 2009; Genge et al., 2018), the cumulative size distribution for CSs from Widerøefjellet (>200 μm size fraction)

was compared to the data provided for a set of CSs from the TAM (>400 μm size fraction; Suavet et al., 2009). The diameters were first collected in 20 μm bins, after which power law functions were fitted to the diameters larger than 240 μm and 440 μm, respectively, to account for potential sieving biases, using the OriginPro software. As the studied size fractions were picked in their entirety, no mathematical corrections were applied. The calculated slope exponent of the TAM cumulative size distribution equals to -4.8 ± 0.2 for the particles larger than 440 μm, in good agreement with values of -4.8 and -5 determined for the non-magnetic and magnetic fractions of the TAM collection (Suavet et al., 2009). The slope exponent of the Widerøefjellet cumulative size distribution equals to -4.4 ± 0.2 (for particles >240 μm), which overlaps within uncertainty with the exponent obtained for the TAM collection (Fig. 4A). These values are close to the -5.0 and -5.4 slopes determined for the SPWW collection (Taylor et al., 2000, 2007b), but may still indicate minor weathering or transport losses for the Widerøefjellet collection. The Walcott Névé collection represents a more extreme case, where a strong deficit in smaller particles not accounted for by a sieving bias (~6% of all CSs > 100 μm is I-type; Table 3) with a large fraction of the MMs exhibiting moderate to severe alteration led to a slope exponent of -2.9 determined for the 200–400 μm size fraction (Suavet et al., 2009). Similarly, the Larkman nunatak collection (~6% of all CSs > 60 μm is I-type) exhibits a power law distribution with an exponent of -5.3 only for diameters from 210 to 330 μm, with abundances decreasing below the power law at both higher and lower diameters (Genge et al., 2018).

Taking into account subtle differences in the classification scheme used for S-type CSs, the relative abundances of Po-, BO-, CC-, and V-type CSs are fairly comparable for the older Larkman nunatak, Cap Prud'homme, and TAM collections on one hand and for the younger Indian Ocean and SPWW collection on the other (Genge et al., 2018). The diversity in quench textures among melted silicate particles has previously been attributed to (i) different peak temperatures and cooling rates experienced during atmospheric entry, with peak temperatures increasing from Po-, over BO- and CC-, to V-type CSs (e.g., Taylor et al., 2000), as supported by the μCT data in this work (Section 3.2), and (ii) the grain size of the precursor material, as coarser-grained micrometeoroids have higher probabilities to evolve into relict-bearing spherules (e.g., Taylor et al., 2012; van Ginneken et al., 2017). Here, it should be noted that the distinction between BO- and CC-type CSs may be biased by the operator, with the existence of a continuum in particle textures and the occurrence of CSs exhibiting dual textures, including mixed BO/CC-type CSs. Based on the comparable abundance of V-type CSs for all collections (except Widerøefjellet), which requires limited subjectivity in classification, such differences have been interpreted to reflect systematic changes in the velocities of the dust particles arriving to Earth (Genge et al., 2018). When comparing the frequency of the different CS types (Table 3), the Widerøefjellet collection is characterized by a significantly higher contribution of V-type CSs for different size fractions above 200 μm. Glass spherules

are generally more prone to fracturing and chemical alteration, mostly due to secondary wind transport and/or strong interaction with ice or fluids over time. This is demonstrated by the heavily altered Walcott Névé and Larkman nunatak collections, where CSs frequently contain surface and penetrative fractures as the result of impact after wind transportation and swelling or cryoclasty (freeze-thaw weathering), respectively (Suavet et al., 2009; van Ginneken et al., 2016; Genge et al., 2018). Although these sites have been accumulating material for at least one Myr, the main factor controlling weathering may be the temperature variation of the local environment, such as seasonal melting of the thin layer of snow covering the MM accumulation sites. The effects of chemical weathering include the removal of primary mineral phases, such as olivine and glass, and incrustations by weathering products (van Ginneken et al., 2016). Ferrihydrite and jarosite have been shown to precipitate within cavities of TAM MMs, resulting in pseudomorphic textures within heavily altered particles. Glass is known to alter into palagonite gels with sequential replacement indicative of varying water-to-rock ratios. Metal may be replaced by Fe-oxide/hydroxide (e.g., goethite, lepidocrocite, and maghemite), although magnetite formed during atmospheric entry is generally resistant to alteration by interaction with the terrestrial environment (van Ginneken et al., 2016).

Physical weathering is mainly due to frequent freeze-thaw cycles occurring due to daily change in surface temperature within the MM traps. Such weathering results in the fracturing of a fraction of the MMs (Rochette et al., 2008; Suavet et al., 2009). In the Widerøefjellet collection, the effects of both chemical and physical weathering of CSs appear limited and similar to what is observed for MMs from the TAM (Tables 1 and 2; Supplementary Table S1), although jarosite weathering products are not abundant (van Ginneken et al., 2016). This is consistent with the assumption of limited variation in the environment over the period of accumulation of the CSs and insubstantial interaction with ice melts. Following the weathering scale for MMs of van Ginneken et al. (2016), based on both the degree of terrestrial alteration and the level of encrustation by secondary phases, the Widerøefjellet particles studied can be assigned to the 0a to 2c scales, indicating no visible to moderate loss and/or alteration of primary material with no visible to complete encrustation (Fig. 3). The limited degree of chemical alteration observed for Widerøefjellet particles may be linked to the high altitude, the presence of a permanent snow layer, or the observation that the CS-rich sediment was sampled in a shadow-rich zone during the peak of the austral Summer.

The bulk geochemical composition of different CS collections can to a certain degree also be used to evaluate possible biases through comparison of the molar $Fe/(Mg + Si)$ ratios of the CSs studied (Fig. 6). Magnetic separation will favor the extraction of magnetite-bearing CSs (e.g., G- and I-type spherules), while non-magnetic V-types will be underrepresented. Hence, CSs with molar $Fe/(Mg + Si)$ above 0.1 ratios will be overrepresented when applying magnetic separation, as observed for the Frontier Mountain and Walcott Névé collections (Suavet et al., 2009).

The molar $Fe/(Mg + Si)$ distribution for a Miller Butte subsample that did not undergo magnetic separation is more similar to that of the SPWW collection (Fig. 6). During the sample preparation of the Widerøefjellet collection, no magnetic or density separation was performed, and the molar $Fe/(Mg + Si)$ ratio distribution is comparable to that of the SPWW (Taylor et al., 2000). Compared to the other collections shown, the Widerøefjellet and SPWW collections both have a significant contribution of particles with molar $Fe/(Mg + Si)$ below 0.1.

Combining the various physicochemical properties of the SRM collection (degree of alteration, abundance by type, size-frequency distribution, $Fe/(Mg + Si)$ ratio, etc.), the Widerøefjellet collection may thus be largely unbiased for the size fractions studied (Table 1; Supplementary Table S1). While the Widerøefjellet collection shares properties with both old and young (Antarctic) MM collections in terms of CSs, the most obvious feature is the high abundance of V-subtype CSs, consistent across different size fractions (Table 3). While secondary trapping and transportation effects, for example due to lack of wind or the presence of a stabilizing fine-grained dust below the snow layer (Genge et al., 2018), cannot be excluded, the high V-subtype abundance, and overall distinct relative abundances of V-, BO-, CC-, and Po-type CSs, in the Widerøefjellet collection could perhaps also be explained by systematic changes in the entry velocities of dust caused by quasi-periodic gravitational perturbation during transport to Earth over the different time periods of CS accumulation. This was first suggested by Genge et al. (2017) to explain the textural differences between recent and older CS collections. Such changes may not be expressed in the Larkman, Cap Prud'homme, TAM and Walcott Névé collections due to higher degrees of weathering or the implementation of magnetic separation techniques.

4.2. Parent body precursors of Widerøefjellet cosmic spherules

4.2.1. Constraints from elemental chemistry

Based on the major element compositions, most, if not all, of the Widerøefjellet particles studied derive from chondritic precursors. This interpretation is based on both major (Figs. 7, 8, 10) and trace (Figs. 9, 10) element compositions and trends, which all indicate compositional ranges close to or within the chondritic fields. This chondritic parentage indicates that the majority of the dust delivered to the Earth samples specific source regions (Section 4.4) and arrives through particular transportation mechanisms (Poynting-Robertson drag for μm to cm particles; Rubin, 2018). The achondritic particles described in literature are thus relatively rare (e.g., Folco and Cordier, 2015). While largely chondritic (e.g., Brownlee et al., 1997), the chemical groups of CSs reflect the degree of heating experienced and the degree of evaporation undergone during atmospheric entry. Decreasing Si/Al and Mg/Al ratios are generally thought to reflect higher degrees of evaporation (e.g., Alexander et al., 2002; Wang et al., 2001) and CSs evolve from the normal group (Si/Al = 14.6 and Mg/Al = 14.2), through the CAT-like group (Si/Al = 9.8 and Mg/Al = 9.9), to the high

Ca–Al group (Si/Al = 6.6 and Mg/Al = 8.0), with variable Fe/Si, Mg/Si, and CaO and Al_2O_3 contents as a result (Taylor et al., 2005; Cordier et al., 2011b; Fig. 8).

The bulk spherule composition is also controlled by the mineralogy of the precursor material (e.g., Imae et al., 2013). This is clear from major element trends, but also from the trace element plots, where the occurrence of specific REE patterns highlights the influence of mineral precursors, such as enstatite and forsterite (Figs. 8D, 9), but possibly also Cr-rich spinel crystals (e.g., WF1202B-0013 and 0041 with >1 wt% Cr_2O_3). As atmospheric melting and concomitant evaporation experienced by CSs strongly affected primary textures, mineralogy and chemical compositions, precisely constraining the nature of the chondritic sources remains highly challenging (e.g., Alexander et al., 2002; Taylor et al., 2005). Most elemental concentrations and ratios are either not sufficiently discriminative or underwent too large a modification to deduce the type of precursor body (e.g., Rudraswami et al., 2016).

4.2.2. Constraints from oxygen isotope ratios

Triple-oxygen isotope ratios have been shown to be a powerful tracer of the origin of CSs and MMs in general (e.g., Engrand et al., 1999; Yada et al., 2005; Taylor et al., 2005; Suavet et al., 2010; Cordier and Folco, 2014). Based on their distribution in three-O isotopic space, bulk CSs have previously been assigned to five large isotopic groups depending on the identification scheme used (Fig. 12; Section 3.5). These assignments take into account mixing with atmospheric oxygen (constant at $\delta^{18}O \approx 23.5‰$ and $\delta^{17}O \approx 11.8‰$ up to 60.9 km altitude; Thiemens et al., 1995) and mass-dependent fractionation during atmospheric entry. Loss of material by evaporation (Engrand et al., 2005) and separation of iron-nickel droplets (Brownlee et al., 1984; Genge and Grady, 1998) may lead to mass-dependent oxygen isotope fractionation with higher $\delta^{17}O$ and $\delta^{18}O$ values (Suavet et al., 2010; Fig. 12). Here, the data collected indicate the existence of a third process affecting the bulk oxygen isotopic compositions of Antarctic CSs, involving the interaction with Antarctic precipitation (Fig. 12). While surface snow samples in Antarctica have revealed highly variable O isotopic compositions, the nearby Nansen blue icefield indicates $\delta^{18}O$ values of $-43 \pm 3‰$ (1 SD; n = 185; Zekollari et al., 2019). Although alteration products of Antarctic CSs vary widely depending on the sample location, exposure age, and textural type of the particles, these will be dominated by Fe-oxyhydroxides, clay minerals, or palagonite (van Ginneken et al., 2016). Alteration products in equilibrium with meteoric waters at 0°C will be offset from the surrounding ice by $\delta^{18}O$ values varying between 0 and 20‰ depending on the minerals concerned (Beaudoin and Therrien, 2009; Alexander et al., 2018), with a secondary mineral assemblage to the right of the surrounding meteoric water along the TFL, with an average $\delta^{18}O$ of roughly $-30‰$. As a result, the bulk composition of the affected CSs will have moved in this general direction (see dashed arrows for *Group 1* extremes on Fig. 12A). This effect is likely important in other collections and previously reported O isotope data as well but remains difficult to

evaluate due to varying preparation and measurement protocols (e.g., washing with aceton versus acid leaching).

Chondritic spherules that plot well below the TFL are commonly assigned to bulk carbonaceous chondrites CV, CO, CM, CR, or their constituent chondrules and refractory inclusions (e.g., Ca-Al-rich inclusions, CAIs). As the isotopic compositions for Wild 2 anhydrous mineral grains partially overlap with the fields defined for both carbonaceous and ordinary chondrites (with $\Delta^{17}O$ between -21.4 and $+3.4‰$ and $\delta^{18}O$ between -47.2 and $+3.5‰$, with 2σ analytical uncertainties ranging from 1 to 4‰ for $\delta^{18}O$; Nakamura et al., 2008), cometary particles cannot be discriminated from asteroidal material. Suavet et al. (2010) discriminated *Group 1* from *Group 2* carbonaceous CSs based on their isotopic signatures (Fig. 12). In this classification scheme, *Group 1* CSs have $\Delta^{17}O \approx -3$ to $-5‰$, and $\delta^{18}O$ in the range of 10-30‰, while *Group 2* CSs have $\Delta^{17}O \approx -1‰$, and $\delta^{18}O$ between 15-35‰. For the Widerøefjellet dataset, only a single CS falls close to the *Group 2* (V-type WF1202B-0057; Table 2; Fig. 12). Fourteen of 16 Widerøefjellet spherules below the TFL plot significantly lower than *Group 2*, extending the ranges of the previously identified *Group 1*, and likely indicate the existence of a continuum between particles deriving from CV, CO, CM and possibly CR carbonaceous chondrites (Fig. 12). Based on mixing lines starting from the chondrite fields, CC-type CS WF1202B-0078 is likely connected to CV carbonaceous chondrites or derives from chondritic refractory inclusions, while V-type WF1202B-0053, BO-type WF1202B-0058, 0064, 0077, and mixed BO/CC-type WF1202B-0080 can conclusively not have a CR chondritic parentage, and share a CV, CO, or CM-related origin (Fig. 12; Table 2).

Group 2 particles, in part linked to CR carbonaceous chondrites, thus constitute only 4% of the Widerøefjellet collection relative to 21% and 17% of similar particles in the TAM and Atacama Desert collections (Suavet et al., 2010; van Ginneken et al., 2017). The cosmic-ray exposure ages for Atacama Desert and TAM surfaces indicate collection windows between the present and 4–5 Myr ago (Suavet et al., 2010; van Ginneken et al., 2017). The measured terrestrial ages of individual TAM particles, based on their thermal remanent magnetization, indicate that most particles (~66%) fell to Earth 1–2 Myr ago, while the remainder (~33%) fell more recently (Suavet et al., 2011b). Thus, in practice, the TAM collection has an accumulation window of up to 2 Ma and is possibly biased toward the latter half of this window. This seems comparable to the collection age for Widerøefjellet, where the deglaciation history of the SRM indicates possible accumulation during the last ~1–3 Ma. This implies that the relative contributions of the O isotopic groups to these collections are not linked to accumulation windows alone, and the observed underrepresentation of *Group 2* particles at Widerøefjellet (Table 2; Fig. 12) may rather reflect the preservation state of the Widerøefjellet collection or the preparation procedures applied before analysis. However, if *Group 2* particles formed from CR chondritic precursors and *Group 1* spherules are dominated by CM-CO-CV carbonaceous chondrites, with the latter much more common than the

CRs in the relatively recent meteorite record (<3 Ma) (Meteoritical Bulletin Database: http://www.lpi.usra.edu/meteor/metbull.php, accessed 17 October 2019), detailed comparison between collections with distinct accumulation windows (e.g., CSs from rooftops; Genge et al., 2017) and analysis of more representative numbers of CSs may reveal changes in the MM source regions.

Particle WF1202B-0071 with a mixed BO-/CC-type texture (Fig. 3) plots slightly below the TFL and to the right of the *Group 2* field ($\Delta^{17}O \approx -0.25\text{‰}$, $\delta^{18}O$ of 37.18‰). Based on its triple-oxygen isotopic composition, WF1202B-0071 may have derived from HED asteroids, or the CI-type or enstatite chondrite parent bodies (Fig. 12). When considering the major element ratios (including Mg/Al, Si/Al, and Fe/Mg) determined using semi-quantitative SEM-EDS before IRMS (Supplementary Fig. S3), this particle likely does not originate from a differentiated parent body and its origin remains ambiguous, as the field for enstatite chondrites overlaps with that of CI chondrites. However, a large degree of mass-dependent isotope fractionation (>30‰) would be required to explain the observed $\delta^{18}O$ from an enstatite chondritic starting composition. Particle WF1202B-0071 could thus potentially originate from a CI chondrite precursor. Based on textural and geochemical observations on unmelted particles, MMs deriving from CI chondrites are known to exist (Kurat et al., 1992; van Ginneken et al., 2012), yet no particles have previously been assigned to CI precursors based on O-isotope data. Such particles are likely more abundant in the smallest size fractions.

Above the TFL, two fairly well-defined groups have been identified that are confirmed by the particles characterized in this work. *Group 3* CSs are mostly related to ordinary chondrites, although contributions from enstatite, R and CI chondrites cannot be excluded (Fig. 12). *Group 4* spherules are characterized by significantly elevated $\delta^{17}O$ and $\delta^{18}O$ (above stratospheric oxygen) and $\Delta^{17}O$ above 1.0‰ (Fig. 12), which have been described as ^{16}O-poor spherules in literature (Yada et al., 2005; Suavet et al., 2010, 2011a,b). To date, the nature of these spherules remains unclear but a derivation from a known ordinary chondritic progenitor appears improbable, as the amount of evaporation required to shift ordinary chondritic compositions towards such high $\delta^{17}O$ and $\delta^{18}O$ does not agree with their measured bulk major element compositions (e.g., Yada et al., 2005; Cordier and Folco, 2014; Supplementary Fig. S3). Instead, fragments of unequilibrated ordinary chondrites, dominated by secondary magnetite grains ($\Delta^{17}O = +5$ to $+7\text{‰}$; Choi et al., 1998) or chondrules with glass or feldspathic mesostasis ($\Delta^{17}O = +3\text{‰}$; Franchi et al., 2001) have been suggested. As all textural subtypes of S-type CSs are represented among the *Group 4* particles studied in this work (V-, CC-, BO-, and Po-type), the latter ideas are no longer considered reasonable, as this would require a magnetite or feldspathic component to be the main contributor to the oxygen isotopic compositions of *Group 4* CSs, which is not tenable considering the modal mineralogy of the particles studied here. Alternatively, these MMs may represent ^{16}O-poor nebular material from a reservoir that currently remains unsampled by normal-sized meteorites (Yada et al., 2005; Suavet et al., 2010). Based on the observed mass-dependent isotope fractionation effects and exchange with atmospheric oxygen for *Group 1* and *Group 3* particles, the probable starting composition of *Group 4* spherules was around $\delta^{18}O \approx +20\text{‰}$ and $\Delta^{17}O \approx +3\text{‰}$, which, albeit large analytical uncertainties, is within range of the bulk O-isotopic measurements reported for particular interplanetary dust particles (IDPs; Starkey et al., 2014).

While metal bead segregation is assumed to induce mass-dependent oxygen isotope fractionation (Genge and Grady, 1998; Suavet et al., 2010), no direct relationship between the presence of high-density phases or high $\delta^{18}O$ is observed for the Widerøefjellet particles, although the nature of the high-density phases (metal bead, sulfide, spinel group mineral, etc.) mostly remains ambiguous (Table 2). This indicates that mass-dependent isotope fractionation may be caused by a variety of processes, including evaporation, high-density phase segregation or kinetic isotope effects during interaction with atmospheric oxygen (Taylor et al., 2005). Similarly, the presence of vesicles does not seem to influence the degree of mass-dependent fractionation experienced (Table 2). While also no correlation is observed between the meteorite type from which the CSs are derived based on oxygen isotope ratios and their chemical group (Cordier et al., 2011b), general trends between the oxygen isotopic composition and textural groups of CSs have previously been observed (van Ginneken et al., 2017) and are discussed in Section 4.4.

4.3. Chemical modification during atmospheric heating

In the following paragraphs, we argue that the observed deviations from chondritic values in bulk chemistry (Figs. 8–11) largely stem from effects linked to evaporation, high-density phase segregation, and redox shifts taking place during atmospheric passage on mostly originally chondritic particles or (refractory) mineral components, rather than from chemical alteration taking place during the terrestrial residence of the studied particles, supporting the pristine nature and representativeness of the Widerøefjellet CS collection. Here, the fragmentation dynamics in specific Solar System source regions, resulting in unrepresentative subsampling of the parent bodies involved, most likely play an important role in determining the bulk composition of CSs.

To study the individual effects of the processes mentioned above, the data for all CS analyzed here are compiled for textural (V-, BO-, and CC-type) and chemical (normal, CAT-like, high Ca-Al) groups, to minimize the effects related to heterogeneity in precursor mineralogy and individual CS chemistry (Table 1; Fig. 10). To obtain an average chemical composition for the normal BO-type CSs, the composition of WF1202B-0013 was excluded, as this normal CS (Fe/Si of 1.09 and Mg/Si of 0.93) is characterized by a high enrichment in REE (average REE$_N$ of 7.03) with a fractionated LREE-enriched pattern ((La/Yb)$_N$ of 3.83), exhibiting negative Ce and Eu anomalies (Supplementary Table S1). Similarly, the composition of WF1202B-0001 was excluded from the high Ca-Al CSs

because of its extreme enrichment in REE (more than 10 times CI) and fractionated REE pattern ((La/Yb)$_N$ of 2.60; Figs. 8, 9; Table 1). Overall, the average REE patterns for the 3 characterized textural (V-, BO-, and CC-type) and chemical (normal, CAT-like, and high Ca-Al) CS groups are consistent with bulk chondrite compositions and exhibit relatively flat REE patterns (La/Yb$_N$ = 0.91–1.01; Table 1; Figs. 8, 9, 10; Supplementary Table S1): 33 out of 34 normal, 6 out of 6 CAT-like, and 3 out of 4 high Ca-Al CSs have relatively chondritic REE patterns (Fig. 9), consistent with literature data (e.g., Folco and Cordier, 2015). With the exception of the LREE-enriched REE patterns recognized in the current work (Fig. 9F), all REE patterns have previously been observed among the 76 V-type spherules of Cordier et al. (2011b). Conversely, U-shaped REE patterns (La/Yb$_N$ = 0.8–2.2; Eu* = 3.8–10.6), the least abundant signature among the V-type spherules of Cordier et al. (2011b), are not observed among the CSs studied here, although perhaps the case could be made that the LREE-enriched patterns observed for WF1202B-0001, 0013, and 0042 (Fig. 9F) partly resemble the U-shaped REE patterns described. A positive Ce anomaly, a feature typical of U-shaped REE patterns (Cordier et al., 2011b), has only been observed in a single V-type spherule (WF1202B-0017) that could also be interpreted to represent a member of the U-shaped group. Likely, a continuum exists between these subtypes, reflecting competing processes linked to the thermal and redox processes taking place during atmospheric passage.

4.3.1. Evaporation

The observed diversity in quench textures and chemical compositions in CSs has previously been interpreted to result from variable peak temperatures and evaporative loss during atmospheric entry and heating (e.g., Taylor et al., 2000; Genge et al., 2008). From Po-type to BO- and CC-type, V-type spherules and then the more strongly evaporated CAT and high Ca-Al spherules, peak temperatures are thought to increase, leading to increases in CaO, Al$_2$O$_3$, TiO$_2$, and MgO contents, as well as decreases in FeO contents relative to chondritic values (Taylor et al., 2000; Cordier et al., 2011b; Section 3.3). These chemical trends are consistent with both geochemical models (Alexander et al. 2002) and experimental simulations (Floss et al., 1996; Wang et al., 2001) of heating and evaporation starting from chondritic and solar compositions (Fig. 11).

By comparing the refractory major element and REE compositions of the CSs with those of the residues obtained after heating of experimental charges with solar composition (Wang et al., 2001), Cordier et al. (2011b) estimated that CSs of the normal group experienced between 40% and 50% mass loss, CAT-like CSs between 50% and 60% mass loss, and high Ca–Al spherules between 80% and 90% mass loss. These calculated values based on the elemental compositions are similar to those estimated for CAT-like spherules based on isotopic values (~50% mass loss; Alexander et al., 2002) and fit with the mass losses of 70–90% proposed by Love and Brownlee (1991), at least for the high Ca-Al CSs. However, these values need to be

considered upper estimates for the mean values, as individual particles can show even larger variations in the degree of evaporation (Fig. 11). According to Taylor et al. (2005), evaporative losses can also be approximated through trends on a plot of the atomic Si/Al versus atomic Mg/Al ratio (Fig. 8D), provided that the bulk composition of the MM precursor can be estimated adequately. Aluminum, with a 50% condensation temperature T$_C$ of 1653 K, is progressively enriched relative to Mg and Si (50% T$_C$ of 1336 K and 1310 K, respectively; Lodders, 2003). Extraterrestrial particles that are progressively evaporated will therefore, follow an evaporation trajectory starting from the carbonaceous and ordinary chondrite source fields. In Fig. 8D, the majority of normal CSs lie within or near the chondrite fields, attesting to minor to moderate degrees of evaporation. The CAT-like and high Ca-Al spherules are positioned further down the evaporation trajectory, which reflects more extreme atmospheric heating conditions. Particle WF1202B-0001 lies at the extreme end of the evaporation curve, with evaporative loss estimates exceeding 90%.

The degree of evaporative loss in CSs during atmospheric entry can also be estimated from refractory trace elements other than the REE (e.g., Sc, Y, Zr, and Hf; Fig. 8C). Refractory trace element contents display a positive correlation with the degree of evaporation and consequently the CaO and Al$_2$O$_3$ contents. While the majority of CSs from the 3 chemical groups fall within a limited range (CaO + Al$_2$O$_3$ < 9 wt%, Sc + Y + Zr + Hf < 33 μg/g) and fairly close to the observed correlation curve with a slope of ~0.27 (Fig. 8C), a number of CSs fall significantly outside this range with strong deviations from the slope (e.g., WF1202B-0001, 0002, 0016, and 0011). The majority of CSs belonging to the normal group are positioned at the lower end of the correlation curve, reflecting minor evaporative losses. In contrast, the CAT-like and high Ca-Al CSs lie at the middle and higher end of the correlation line, suggesting ~50% and >75% mass losses, respectively. Particle WF1202B-0001 is an extreme case positioned at the far end of the correlation line, again indicating strong evaporative loss (~90%). While this particle may have been affected by some terrestrial alteration, the elements used in Fig. 8C are relatively immobile and should only undergo limited effects from such process. As the slope of the correlation curve is defined by the volatility of the combination of elements considered, CSs that deviate from this trend may reflect highly variable precursor mineralogy and geochemistry (e.g., Imae et al., 2013).

4.3.2. Depletion in siderophile and chalcophile elements

Both siderophile (including W, Co, Ni) and chalcophile (including V, Cr, Mn) trace elements show systematic negative anomalies relative to their neighboring lithophile elements when ordered according to increasing volatility (Fig. 10). In the CSs studied in this work, the depletion in siderophile elements is most pronounced for CAT-like CSs, while the high Ca-Al spherules exhibit siderophile element depletions of similar magnitude as those observed for normal CSs. Among normal CSs, the depletions are comparable for CC- and V-type spherules, while the effects are less

pronounced for BO-type spherules (Table 2; Fig. 10). The depletions relative to chondritic values observed for chalcophile elements are comparable for CAT-like and high Ca-Al CSs, but less pronounced in normal CSs.

Relative to experimentally defined evaporation trends, CAT-like spherules, presumably affected by intermediate degrees of evaporative loss, display FeO concentrations significantly lower than those measured for the high Ca–Al and normal groups (Figs. 10, 11D–F; Cordier et al., 2011b). This confirms that Fe concentrations in CSs are not only governed by the evaporation process. This is consistent with the Fe isotope fractionation observed in CSs, indicating that Fe is mainly lost by physical separation of metal-rich phases, with minor free evaporation, except perhaps in the case of CAT-like and high Ca-Al spherules (Alexander et al., 2002; Engrand et al., 2005; Taylor et al., 2005).

The data reported here confirm the observations of Cordier et al. (2011b) who propose that mechanical separation of siderophile- and chalcophile-rich phases occurs during atmospheric entry, rather than partitioning of chalcophile elements into metal phases or loss by evaporation alone (Brownlee et al., 1997; Genge and Grady, 1998). While removal of Fe–Ni metal or sulfide beads from silicate melts has long been considered to cause depletions in siderophile and possibly chalcophile elements (e.g., Brownlee et al., 1997; Genge and Grady, 1998), the separation of chalcophile-rich solids, such as chromites, is a more recent idea (Cordier et al., 2011b). The latter authors suggest that the migration of chromite grains toward the particle periphery may result from differential acceleration between contained chromite grains and silicate melt, or as proposed for metal beads in spinning CSs from centrifugal forces or floating of chromite grains on rising vesicles, as surface tension allows for their fixation on the vesicle surface. However, the density range for chromite between 4.5 and 5 g/cm^3 perhaps renders the latter unlikely.

As chromite is a potential refractory phase in basaltic melts (e.g., Longhi and Pan, 1988; Roeder and Reynolds, 1991), incomplete melting during atmospheric heating could lead to a depletion of chalcophile elements in silicate melts. When chromite grains are small, their melting may take place relatively fast, while the contrast in density relative to silicate melt may be less effective and inhibit settling (Genge et al., 2016). However, if chalcophile and siderophile element depletions result from (refractory) metal, sulfide or spinel group mineral losses, then the enrichment in siderophile and to lesser extent chalcophile elements observed in high Ca-Al CSs would require that these particles underwent less efficient separation of such high-density phases during atmospheric passage, relative to the other chemical CS groups. As high Ca-Al spherules are interpreted to have experienced the highest evaporative losses and peak temperatures, their enrichment in siderophile and chalcophile elements relative to spherules that formed at lower temperatures may simply result from the oversampling of more refractory phases within the MM, i.e., a slight excess of spinel group minerals or refractory metal nuggets (e.g., as in the refractory Ir and Pt-enriched high Ca-Al WF1202B-0011) rather than high-density phase ejection.

4.3.3. Effects from redox conditions

Following the work of Cordier et al. (2011b) on V-type spherules and extending these observations to BO-type and CC-type CSs, the CS compositions determined here can be compared to those of residues obtained after heating of experimental charges with solar composition in terms of refractory major element and REE compositions (Fig. 11; Wang et al., 2001; Cordier et al., 2011b). The progressive enrichment observed for refractory REEs from the normal group (avg. $REE_N = 1.8 \times CI$) over the CAT-like group (avg. $REE_N = 4.1 \times CI$) to the high Ca–Al group (avg. $REE_N = 4.5 \times CI$; Table 2) is consistent with increasing levels of evaporation. Evaporation mostly does not fractionate the REEs, yet Ce does not always occur in chondritic proportions in CSs (Figs. 9, 11). While some of the observed Ce anomalies may be linked to terrestrial alteration (e.g., WF1202B-0013 and 0017), this is unlikely to be the case for all particles studied here, as most are relatively fresh, devoid of fracturing and surficial alteration. In addition, the CSs showing Ce depletions are not equally distributed among the different chemical groups studied, with 83% (by number) of the CAT-like, 67% of the high Ca-Al, and only 15% of the normal chondritic CSs exhibiting REE patterns characterized by a negative Ce anomaly (with Ce* < 0.88; Figs. 9, 11). While experimental residues systematically show large negative anomalies in Ce for mass losses larger than 50% (Floss et al., 1996; Wang et al., 2001), Ce anomalies observed in CSs are generally smaller in magnitude (1–2 versus 3 orders of magnitude in experiments; Fig. 11). As these Ce anomalies are thought to result from the volatile behavior of Ce^{4+} under highly oxidizing conditions prevalent during non-equilibrium kinetic evaporation in Earth's atmosphere (Hashimoto, 1990; Floss et al., 1996; Wang et al., 2001), Ce depletions in CSs hint at moderately oxidizing conditions during atmospheric passage or incomplete vacuum during the experiments. As the Ce anomalies are mainly observed in CAT-like and high Ca–Al spherules that are interpreted to have experienced mass losses of 50% or higher, Ce anomalies in CSs may relate to high degrees of evaporation experienced during atmospheric entry, which could allow for local increases in the partial pressure of oxygen (Cordier et al., 2011b).

4.4. Comparison to other Antarctic micrometeorite collections and implications for the interplanetary dust complex

While major and trace element concentrations indicate a largely chondritic parentage for the CSs studied in this work, oxygen isotope ratios can refine the relative contributions of each chondrite class. Cordier and Folco (2014) compiled previously reported three-oxygen isotope data for 136 CSs. Of these 136 spherules, ranging from 50 μm to 2280 μm in diameter and studied using both IRMS and ion microprobe, ~60% relate to carbonaceous chondrite asteroids (or comets), ~17% to ordinary chondrites, ~8% to a ^{16}O-poor reservoir, and ~4% to HED asteroids, while ~11% remain ambiguous. Importantly, the ratio of carbonaceous chondrite relative to ordinary chondrite material decreases as the CS diameter increases, from ~10 for small

Table 4

Parentage statistics for 28 silicate cosmic spherules determined in this work, compared to previously compiled literature data (Cordier and Folco, 2014).

Groups[a]	OC-related	CC-related	^{16}O-poor	Ambiguous	HED-related	Total[b]
# of spherules in this work	8	15	4	1	0	28
% all sizes	29	54	14	4	0	
% 250–500 μm	29	57	7	7	0	14
% 500–1000 μm	29	50	21	0	0	14
% V-type	50	40	10	0	0	10
% BO-type	14	71	14	0	0	7
% Po-type	0	50	50	0	0	2
% CC-type	17	67	17	0	0	6
# of spherules in literature	23	81	11	15	6	136
% all sizes	17	60	8	11	4	
% <100 μm	7	66	17	10	0	29
% 100–250 μm	6	68	10	16	0	31
% 250–500 μm	9	80	6	6	0	35
% 500–1000 μm	38	38	0	6	19	32
% > 1000 μm	44	11	11	33	0	9

[a] The proportion of CSs assigned to the ambiguous group provides some indication on the degree of certainty in the assignment of particles to these isotopic groups.

[b] Totals are expressed as the number of spherules.

particles (<500 μm) to ~0.3 for particles larger than 500 μm. For CSs in the range of 500–1000 μm (32 in the compiled dataset), ~38% can be linked to ordinary chondrites, while ~38% relate to carbonaceous chondrites, ~6% remain ambiguous and ~19% are related to HED asteroids (Table 4). Note that the latter were the focus of the work by Cordier et al. (2011a) and the particles analyzed were selected based on their chemical composition, leading to a population bias. In the 250–500 μm size fraction, the number of CSs in the literature linked to ordinary chondrites decreases to ~9%, while those related to carbonaceous chondrites increase to ~80%, with ^{16}O-poor and ambiguous CSs both contributing ~6% of the population. Cosmic spherules below 500 μm are composed of ~70% carbonaceous chondrite-derived material (Cordier and Folco, 2014), consistent with the Mg-Si-Al compositions of various MM collections (Taylor et al., 2012; Genge, 2008). This distribution indicates that a significant proportion of large (>200 μm) MMs are related to ordinary chondrites or to CO, CV, CK carbonaceous chondrites, whereas smaller MMs (from 20 to 100 μm) are mainly linked to CM2 or CR2 chondrites (Kurat et al., 1994; Brownlee et al., 1997; Engrand and Maurette, 1998; Engrand et al., 2005). This relationship may reflect the lower mechanical resistance of phyllosilicate-bearing chondrites, leading to enhanced fragmentation into smaller particles during dust production in space as a result of the collisions between their parent asteroids (Flynn et al., 2009). Examples of large anhydrous chondritic MMs include a >1000 μm CV-like and a >700 μm CK-like MM (van Ginneken et al., 2012; Cordier et al., 2018). However, exceptions exist, as illustrated by unambiguously hydrated fine-grained chondritic CM/CR MMs recovered from the >400 μm size fraction (Suttle et al., 2019).

For Widerøefjellet, a fairly similar particle parentage is observed for the 500–1000 μm size fraction, with ~50% of the spherules relating to carbonaceous chondrites, ~29%

to ordinary chondrites, and ~21% to ^{16}O-poor material. Although the set of analyzed CSs remains limited, no clear population shift is observed for the 250–500 μm size fraction (~29% OC, ~57% CC, ~7% ^{16}O-poor, 7% ambiguous; Table 4). However, it should be noted that most of the CSs characterized in this size fraction fall between ~400 and 500 μm, so the expected transition in terms of relative abundance between the two CS size populations at around 500 μm (Cordier and Folco, 2014) might in fact lie between 250 and 400 μm. This agrees with impact destruction experiments on hydrous (e.g., CM chondrite) and anhydrous (e.g., ordinary chondrite) targets that show that small dust particles less than 300 μm are favored in hydrous (carbonaceous) targets (Flynn et al., 2009).

In the compilation of Cordier and Folco (2014), no correlation was observed between CS texture and their assigned precursor material, except that most spherules related to HED asteroids primarily belong to the V-type subtype. Van Ginneken et al. (2017) recently studied a number of CSs recovered from the Atacama Desert and compared these to TAM CSs to determine possible relationships between the different textural CS types and their respective parent bodies. These authors concluded that coarse-grained dust particles, with affinities toward the ordinary chondrite parent bodies, are more prone to produce Po textures. At higher peak temperatures, these dust particles will preferably develop a CC-type texture, rather than a BO texture, due to the lack of nuclei available to develop new crystal faces. In contrast, BO spherules are predominantly thought to originate from the matrices of fine-grained carbonaceous chondrite particles (van Ginneken et al., 2017). This is mainly attributed to the mineralogical variety present in the matrices of carbonaceous chondrites, favoring supercooling, as well as the presence of accessory mineral phases, which may act as nuclei for the development of BO textures. No correlations have been found for V-type spherules as the highest peak

temperatures ensure complete melting of the MM precursor, regardless of composition. Based on the triple-oxygen isotopic data of the Widerøefjellet collection (Table 2), the predominance of BO-type CSs toward a carbonaceous chondrite precursor (71% of BO-type), and the lack of correlation between V-type spherules and a specific precursor is confirmed. Yet, Po- and CC-type spherules do not follow the trends mentioned above. More specifically, one Po-type CS appears to be related to the *Group 4* CSs, while another is linked to carbonaceous chondrites (Tables 2 and 4). CC-type spherules at Widerøefjellet have a predominant affinity with carbonaceous chondrites (67%), as opposed to ordinary chondrites (17%). *Group 4* CSs are represented by all four major textural types. Hence, accurate predictions of the parent body composition of CSs solely based on textural properties remains challenging.

The oxygen isotope composition of the SRM CS collection confirms that the composition of the micrometeoroid complex is different from that of macroscopic meteoroids. Materials with compositions similar to CI, CR, CM, CV, and CO chondrites dominate the former, whereas ordinary chondrites ($\sim$86%) and evolved meteorites (e.g., HED, making up $\sim$4%) dominate the latter (Meteoritical Bulletin Database: http://www.lpi.usra.edu/meteor/metbull.php, accessed 17 October 2019). Cosmic spherule statistics thus indicate that asteroids commonly observed in the inner asteroid belt (e.g., S-type ordinary chondrite and V-type HED parent asteroids) feed 20–30% or more of the micrometeoroid complex (Table 4). The other 55–60% are related to primitive solar system objects with carbonaceous chondritic compositions (Cordier and Folco, 2014). These materials could be associated to silicate dust released by short-period comets (e.g., Nesvorný et al., 2010) or with primitive asteroids belonging to the C-, D- or P-type spectral classes in the middle and outer asteroid belt (from 2.8 AU to Jupiter's orbit). In the case of the latter, recently disrupted asteroid families represent the primary source of MMs. Based on dynamic modeling and observations using the Infrared Astronomical Telescope (IRAS), three major dust bands produced by the C-type Veritas, older C-type Themis, and S(IV)-type Koronis asteroid families supply the majority of asteroidal dust delivered to the Earth (Kortenkamp, 1998; Nesvorný et al., 2002; Genge, 2008). Continued oxygen isotope ratio work on CSs, and MMs in general, extending the numbers of characterized particles as well as the currently sampled size fractions, will lead to a more refined understanding of the contributions of the various parent bodies in the solar system to the different fractions of the extraterrestrial flux to Earth and more accurately point out possible fluctuations with time.

5. CONCLUSIONS

To demonstrate the representativeness of the Widerøefjellet CS collection, the physicochemical properties of the CSs in this deposit, including cumulative size distribution, frequency by type and chemical composition, presence of vesicles and high-density phases, major and trace element chemical compositions, and oxygen isotope ratios, have been compared to those of other Antarctic MM deposits, including the TAM and SPWW collections. Although the Widerøefjellet deposit contains unmelted and scoriaceous MMs (<5% of all MMs) as well as both silicate- and metal-rich CSs ($\sim$95% and $\sim$5% of all CSs, respectively), this work focused on characterizing the silicate-rich CSs larger than 200 μm. All major textural (V-, BO-, CC-, and Po-type) and chemical (normal, CAT-like, high Ca-Al) CS groups are present. Most particles appear relatively unaltered, while the proportions for each CS type are comparable to those of the least biased Antarctic collections. While the molar Fe/(Mg + Si) ratios of the studied CSs are similar to that of the SPWW, a higher proportion of V-type CSs relative to other deposits was found. A relatively unbiased cumulative size distribution plot supports the claim of an essentially representative MM deposit. The -4.4 exponent slope of the size distribution is similar to that of the TAM collection, suggesting direct infall to be the dominant process controlling the MM accumulation. The widely varying degree of alteration for Widerøefjellet and TAM particles, from fresh to heavily altered, confirms the long accumulation ranges from respectively $\sim$3 and $\sim$4 Myr ago to present.

A subset of Widerøefjellet CSs larger than 325 μm was characterized for major and trace element concentrations and oxygen isotope ratios. The collected data confirm the major trends observed in literature, linking the Widerøefjellet CSs to chondritic precursors and their mineralogical constituents, which underwent chemical changes during atmospheric passage. Various factors control the CS composition, including the primary characteristics of the parent body precursors, the presence and expulsion of high-density phases (including metal bead, sulfides, and spinel crystals) as well as evaporation linked to differential redox and thermal conditions following atmospheric entry, and subsequent terrestrial alteration. The parent bodies of MMs are thought to differ from those sampled by normal-sized meteorites due to different production and transport mechanisms. At least 50% by number of CSs from all size fractions relate to primitive solar system objects with carbonaceous chondrite compositions, either to the C-, D-, or P-type spectral class asteroids in the outer asteroid belt or, alternatively, to comets. The contribution of ordinary chondrite particles shows larger variations, and strongly depends on the size fraction of the particles studied. A relatively constant proportion of CSs ($\sim$10%) is related to a chondritic reservoir depleted in ^{16}O. Overall, the physicochemical properties of the Widerøefjellet particles denote a distinctive and representative collection of CSs from East Antarctica, including a statistically significant number of particles with diameters larger than 800 μm. The Widerøefjellet collection complements currently existing collections and offers an important addition to study the composition of the MM flux over the last few million years.

Declaration of Competing Interest

The authors declare that they have no known competing financial interests or personal relationships that could have appeared to influence the work reported in this paper.

APPENDIX A. SUPPLEMENTARY MATERIAL

Supplementary data to this article can be found online at https://doi.org/10.1016/j.gca.2019.11.016.

REFERENCES

Alexander C. M. O., Taylor S., Delaney J. S., Ma P. and Herzog G. F. (2002) Mass-dependent fractionation of Mg, Si, and Fe isotopes in five stony cosmic spherules. *Geochim. Cosmochim. Acta* **66**, 173–183.

Alexander C. M. O., Greenwood R. C., Bowden R., Gibson J. M., Howard K. T. and Franchi I. A. (2018) A multi-technique search for the most primitive CO chondrites. *Geochim. Cosmochim. Acta* **221**, 406–420.

Beaudoin G. and Therrien P. (2009) The updated web stable isotope fractionation calculator. In *Handbook of Stable Isotope Analytical Techniques* (ed. P. A. DeGroot). Elsevier, Amsterdam, Netherlands, pp. 1120–1122.

Blanchard M. B., Brownlee D. E., Bunch T. E., Hodge P. W. and Kyte F. T. (1980) Meteoroid ablation spheres from deep-sea sediments. *Earth Planet. Sci. Lett.* **46**, 178–190.

Brownlee, D. E., Pilachowski, L. B. and Hodge, P. W. (1979) Meteorite mining on the ocean floor. Lunar Planet. Sci. Conf. X. Lunar Planet. Inst., Houston. #157–158 (abstr.).

Brownlee D. E., Bates B. A. and Wheelock M. M. (1984) Extraterrestrial platinum group nuggets in deep-sea sediments. *Nature* **309**, 693–695.

Brownlee D. E., Bates B. and Schramm L. (1997) The elemental composition of stony cosmic spherules. *Meteorit. Planet. Sci.* **32**, 157–175.

Choi B.-G., McKeegan K. D., Krot A. N. and Wasson J. T. (1998) Extreme oxygen-isotope compositions in magnetite from unequilibrated ordinary chondrites. *Nature* **392**, 577–579.

Clayton R. N. (1993) Oxygen isotopes in meteorites. *Annu. Rev. Earth Planet. Sci.* **21**, 115–149.

Clayton R. N. and Mayeda T. K. (1999) Oxygen isotope studies of carbonaceous chondrites. *Geochim. Cosmochim. Acta* **63**, 2089–2104.

Clayton R. N., Mayeda T. K., Olsen E. J. and Goswami J. N. (1991) Oxygen isotope studies of ordinary chondrites. *Geochim. Cosmochim. Acta* **55**, 2317–2337.

Cordier C. and Folco L. (2014) Oxygen isotopes in cosmic spherules and the composition of the near Earth interplanetary dust complex. *Geochim. Cosmochim. Acta* **146**, 18–26.

Cordier C., Folco L. and Taylor S. (2011a) Vestoid cosmic spherules from the South Pole Water Well and Transantarctic Mountains (Antarctica): A major and trace element study. *Geochim. Cosmochim. Acta* **75**, 1199–1215.

Cordier C., Folco L., Suavet C., Sonzogni C. and Rochette P. (2011b) Major, trace element and oxygen isotope study of glass cosmic spherules of chondritic composition: The record of their source material and atmospheric entry heating. *Geochim. Cosmochim. Acta* **75**, 5203–5218.

Cordier C., Suavet C., Folco L., Rochette P. and Sonzogni C. (2012) HED-like cosmic spherules from the Transantarctic Mountains, Antarctica: Major and trace element abundances and oxygen isotopic compositions. *Geochim. Cosmochim. Acta* **77**, 515–529.

Cordier C., Baecker B., Ott U., Folco L. and Trieloff M. (2018) A new type of oxidized and pre-irradiated micrometeorite. *Geochim. Cosmochim. Acta* **233**, 135–158.

Dartois E., Engrand C., Brunetto R., Duprat J., Pino T., Quirico E., Remusat L., Bardin N., Briani G., Mostefaoui S., Morinaud G., Crane B., Szwec N., Delauche L., Jamme F., Sandt Ch. and Dumas P. (2013) Ultracarbonaceous Antarctic micrometeorites, probing the Solar System beyond the nitrogen snowline. *Icarus* **224**, 243–252.

Dobrică, E., Engrand, C., Duprat, J. and Gounelle, M. (2010) A statistical overview of Concordia Antarctic micrometeorites. In 73rd Ann. Meet. of Meteorit. Soc. New York, N.Y., USA. #5213 (abstr.).

Dobrică E., Engrand C., Leroux H., Rouzaud J.-N. and Duprat J. (2012) Transmission electron microscopy of CONCORDIA UltraCarbonaceous Antarctic MicroMeteorites (UCAMMs): Mineralogical properties. *Geochim. Cosmochim. Acta* **76**, 68–82.

Duprat J., Maurette M., Engrand C., Matrajt G., Immel G., Gounelle M. and Kurat G. (2001) An estimation of the contemporary micrometeorite flux obtained from surface snow samples collected in central Antarctica. *Meteorit. Planet. Sci.* **36**. A52 (abstr.).

Duprat J., Engrand C., Maurette M., Kurat G., Gounelle M. and Hammer C. (2007) Micrometeorites from central Antarctic snow: The CONCORDIA collection. *Adv. Space Res.* **39**, 605–611.

Duprat J., Dobrica E., Engrand C., Aleon J., Marrocchi Y., Mostefaoui S., Meibom A., Leroux H., Rouzaud J.-N., Gounelle M. and Robert F. (2010) Extreme deuterium excesses in Ultracarbonaceous Micrometeorites from central Antarctic snow. *Science* **328**, 742–745.

Engrand C. and Maurette M. (1998) Carbonaceous micrometeorites from Antarctica. *Meteorit. Planet. Sci.* **33**, 565–580.

Engrand C., McKeegan K. D. and Leshin L. (1999) Oxygen isotopic compositions of individual minerals in Antarctic

micrometeorites: Further links to carbonaceous chondrites. *Geochim. Cosmochim. Acta* **63**, 2623–2636.

Engrand C., McKeegan K. D., Leshin L. A., Herzog G. F., Schnabel C., Nyquist L. E. and Brownlee D. E. (2005) Isotopic compositions of oxygen, iron, chromium, and nickel in cosmic spherules: toward a better comprehension of atmospheric entry heating effects. *Geochim. Cosmochim. Acta* **69**, 5365–5385.

Floss C., Goresy A. E., Zinner E., Kransel G., Rammensee W. and Palme H. (1996) Elemental and isotopic fractionations produced through evaporation of the Allende CV chondrite: implications for the origin of HAL-type hibonite inclusions. *Geochim. Cosmochim. Acta* **60**, 1975–1997.

Flynn G. J., Durda D. D., Sandel L. E., Kreft J. W. and Strait M. M. (2009) Dust production from the hypervelocity impact disruption of the Murchison hydrous CM2 meteorite: Implications for the disruption of hydrous asteroids and the production of interplanetary dust. *Planet. Space Sci.* **57**, 119–126.

Folco L. and Cordier C. (2015) Micrometeorites. In *EMU Notes in Mineralogy 15: Planetary Mineralogy* (eds. M. R. Lee and H. Leroux). European Mineralogical Union, Twickenham, United Kingdom, pp. 253–297.

Folco L., Rochette P., Perchiazzi N., D'Orazio M., Laurenzzi M. and Tiepolo M. (2008) Microtektites from Victoria Land Transantarctic Mountains. *Geology* **36**, 291–294.

Folco L., D'Orazio M., Tiepolo M., Tonarini S., Ottolino L., Perchiazzi N. and Rochette P. (2009) Transantarctic Mountain microtektites: geochemical affinity with Australasian microtektites. *Geochim. Cosmochim. Acta* **73**, 3694–3722.

Franchi I. A., Wright I. P., Sexton A. S. and Pillinger C. T. (1999) The oxygen-isotopic composition of Earth and Mars. *Meteorit. Planet. Sci.* **34**, 657–661.

Franchi I. A., Baker L., Bridges J. C., Wright I. P. and Pillinger C. T. (2001) Oxygen isotopes and the early solar system. *Philos. Trans. R. Soc. A* **359**, 2019–2035.

Fredriksson K. and Martin L. R. (1963) The origin of black spherules found in Pacific islands, deep sea sediments, and Antarctic ice. *Geochim. Cosmochim. Acta* **27**, 245–248.

Friedrich J. M., Wang M.-S. and Lipschutz M. E. (2002) Comparison of the trace element composition of Tagish Lake with other primitive carbonaceous chondrites. *Meteorit. Planet. Sci.* **37**, 677–686.

Ganapathy R., Brownlee D. E. and Hodge P. W. (1978) Silicate spherules from deep sea sediments: Confirmation of extraterrestrial origin. *Science* **201**, 1119–l121.

Genge M. J. (2008) Koronis asteroid dust within Antarctic ice. *Geology* **36**, 687–690.

Genge M. J. and Grady M. M. (1998) Melted micrometeorites from Antarctic ice with evidence for the separation of immiscible Fe–Ni–S liquids during entry heating. *Meteorit. Planet. Sci.* **33**, 425–434.

Genge M. J. and Grady M. M. (1999) The fusion crusts of stony meteorites: implications for the atmospheric reprocessing of extraterrestrial materials. *Meteorit. Planet. Sci.* **34**, 341–356.

Genge M. J., Grady M. M. and Hutchison R. (1997) The textures and compositions of fine-grained Antarctic micrometeorites – Implications for comparisons with meteorites. *Geochim. Cosmochim. Acta* **61**, 5149–5162.

Genge M. J., Engrand C., Gounelle M. and Taylor S. (2008) The classification of micrometeorites. *Meteorit. Planet. Sci.* **43**, 497–515.

Genge M. J., Suttle M. and van Ginneken M. (2016) Olivine settling in cosmic spherules during atmospheric deceleration: An indicator of the orbital eccentricity of interplanetary dust. *Geophys. Res. Lett.* **43**, 10646–10653.

Genge M. J., Larsen J., Suttle M. D. and van Ginneken M. (2017) An urban collection of modern-day large micrometeorites:

Evidence for variations in the extraterrestrial dust flux through the Quaternary. *Geology* **45**, 119–122.

Genge M. J., van Ginneken M., Suttle M. D. and Harvey R. P. (2018) Accumulation mechanisms of micrometeorites in an ancient supraglacial moraine at Larkman Nunatak, Antarctica. *Meteorit. Planet. Sci.* **53**, 2051–2066.

Gorodetskaya I. V., Van Lipzig N. P. M., Van den Broeke M. R., Mangold A., Boot W. and Reijmer C. H. (2013) Meteorological regimes and accumulation patterns at Utsteinen, Dronning Maud Land, East Antarctica: Analysis of two contrasting years. *J. Geophys. Res.-Atmos.* **118**, 1–16.

Goodrich C. A. and Delaney J. S. (2000) Fe/Mg-Fe/Mn relations of meteorites and primary heterogeneity of primitive achondrite parent bodies. *Geochim. Cosmochim. Acta* **64**, 149–160.

Gounelle M., Engrand C., Maurette M., Kurat G., McKeegan K. D. and Brandstätter F. (2005) Small Antarctic micrometeorites: A mineralogical and in situ oxygen isotopic study. *Meteorit. Planet. Sci.* **40**, 917–932.

Gounelle M., Chaussidon M., Morbidelli A., Barrat J.-A., Engrand C., Zolensky M. E. and McKeegan K. D. (2009) A unique basaltic micrometeorite expands the inventory of solar system planetary crusts. *Proc. Natl. Acad. Sci. USA* **106**, 6904–6909.

Greenwood R. C., Schmitz B., Bridges J. C., Hutchison R. and Franchi I. A. (2007) Disruption of the L chondrite parent body: new oxygen isotope evidence from Ordovician relict chromite grains. *Earth Planet. Sci. Lett.* **262**, 204–213.

Greenwood R. C., Burbine T. H., Miller M. F. and Franchi I. A. (2017) Melting and differentiation of early-formed asteroids: The perspective from high precision oxygen isotope studies. *Chem. Erde-Geochem.* **77**, 1–43.

Hagen E. H., Koeberl C. and Faure G. (1989) Extra-terrestrial spherules in glacial sediment, Beardmore-Glacier area, Transantarctic Mountains. *Contrib. Antarct. Res. I Antarct. Res. Ser.* **50**, 19–24.

Harvey R. P. and Maurette M. (1991) The origin and significant of cosmic dust from Walcott Névé, Antarctica. *Proc. Lunar Planet. Sci. Conf.* **21**, 569–578.

Hashimoto A. (1990) Evaporation kinetics of forsterite and implications for the early solar nebula. *Nature* **347**, 53–55.

Imae N., Taylor S. and Iwata N. (2013) Micrometeorite precursors: Clues from the mineralogy and petrology of their relict minerals. *Geochim. Cosmochim. Acta* **100**, 113–157.

Imae N., Debaille V., Akada Y., Debouge W., Goderis S., Hublet G., Mikouchi T., Van Roosbroek N., Yamaguchi A., Zekollari H., Claeys Ph. and Kojima H. (2015) Report of the JARE-54 and BELARE 2012–2013 joint expedition to collect meteorites on the Nansen Ice Field, Antarctica. *Antarct. Rec.* **59**, 38–72.

Jarosewich E. (1990) Chemical analysis of meteorites: A compilation of stony and iron meteorite analyses. *Meteoritics* **25**, 323–337.

Kamei A., Horie K., Owada M., Yuhara M., Nakano N., Osanai Y., Adachi T., Hara Y., Terao M., Teuchi S., Shimura T., Tsukada K., Hokada T., Iwata C., Shiraishi K., Ishizuka H. and Takahashi Y. (2013) Late Proterozoic juvenile arc metatonalite and adakitic intrusions in the Sør Rondane Mountains, eastern Dronning Maud Land, Antarctica. *Precambrian Res.* **234**, 47–62.

Koeberl C. and Hagen E. H. (1989) Extraterrestrial spherules in glacial sediment from the Transantarctic Mountains, Antarctica: Structure, mineralogy, and chemical composition. *Geochim. Cosmochim. Acta* **53**, 937–944.

Kojima S. and Shiraishi K. (1986) Note on the geology of the western part of the Sør Rondane Mountains, East Antarctica. *Mem. Natl. Inst. Polar Res.* **43**, 116–131.

Kortenkamp S. J. (1998) Accretion of interplanetary dust particles by the Earth. *Icarus* **135**, 469–495.

Kurat G., Presper T., Brandstätter F., Maurette M. and Koeberl C. (1992) CI-like micrometeorites from Cap-Prudhomme, Antarctica. *Lunar Planet. Sci. Conf. XXIII. Lunar Planet. Inst.* Houston, 747–748.

Kurat G., Koeberl C., Presper T., Brandstätter F. and Maurette M. (1994) Petrology and geochemistry of Antarctic micrometeorites. *Geochim. Cosmochim. Acta* **58**, 3879–3904.

Love S. G. and Brownlee D. E. (1991). Heating and thermal transformation of micrometeoroids entering the Earth's atmosphere. *Icarus* **89**, 26–43.

Lodders K. (2003) Solar system abundances and condensation temperatures of the elements. *Astrophys. J.* **591**, 1220–1247.

Longhi J. and Pan V. (1988) A reconnaissance study of phase boundaries in low-alkali basaltic liquids. *J. Petrol.* **29**, 115–147.

Love S. G. and Brownlee D. E. (1993) A direct measurement of the terrestrial mass accretion rate of cosmic dust. *Science* **262**, 550–553.

Martin C., Debaille V., Lanari P., Goderis S., Vandendael I., Vanhaecke F., Vidal O. and Claeys Ph. (2013) REE and Hf distribution among mineral phases in the CV–CK clan: A way to explain present-day Hf isotopic variations in chondrites. *Geochim. Cosmochim. Acta* **120**, 496–513.

Masschaele B. C., Cnudde V., Dierick M., Jacobs P., Van Hoorebeke L. and Vlassenbroeck J. (2007) UGCT: New X-ray radiography and tomography facility. *Nucl. Instrum. Meth. A* **580**, 266–269.

Masschaele B. C., Dierick M., Loo D. V., Boone M. N., Brabant L., Pauwels E., Cnudde V. and Hoorebeke L. V. (2013) HECTOR: A 240kV micro-CT setup optimized for research. *J. Phys. Conf. Ser.* **463**(1). https://doi.org/10.1088/1742-6596/463/1/012012 012012.

Maurette M., Immel G., Hammer C., Harvey R., Kurat G. and Taylor S. (1994) Collection and curation of IDPs from the Greenland and Antarctic ice sheets. In *Analysis of Interplanetary Dust Conference Proceedings* (eds. M. E. Zolensky, T. L. Wilson, F. J. M. Rietmeijer and G. J. Flynn). Am. Inst. Phys, Houston, pp. 277–289.

McDonough W. F. and Sun S. S. (1995) The composition of the Earth. *Chem. Geol.* **120**, 223–253.

Miller M. F., Franchi I. A., Sexton A. S. and Pillinger C. T. (1999) High precision $\delta^{17}O$ isotope measurements of oxygen from silicates and other oxides: method and applications. *Rapid Commun. Mass Sp.* **13**, 1211–1217.

Moriwaki K., Hirakawa K. and Matsuoka N. (1991) Weatering stafe of till and glacial history of the central Sør Rondane Mountains, East Antarctica. *Proc. NIPR. Sym. Antarct. Geosci.* **5**, 99–111.

Nakamura T., Imae N., Nakai I., Noguchi T., Yano H., Terada K. and Ohmori R. (1999) Antarctic micrometeorites collected at the Dome Fuji Station. *Antarct. Meteorite Res.* **12**, 183–198.

Nakamura T., Noguchi T., Tsuchiyama A., Ushikubo T., Kita N. K., Valley J. Y., Zolensky M. E., Kakazu Y., Sakamoto K., Mashio E., Uesugi K. and Nakano T. (2008) Chondrule-like objects in short-period comet 81P/Wild 2. *Science* **321**, 1664–1667.

Nesvorný D., Bottke W. F., Dones L. and Levison H. F. (2002) The recent breakup of an asteroid in the main-belt region. *Nature* **417**, 720–771.

Nesvorný D., Jenniskens P., Levison H. F., Bottke W. F., Vokrouhlicky D. and Gounelle M. (2010) Cometary origin of the zodiacal cloud and carbonaceous micrometeorites. Implications for hot debris disks. *Astrophys. J.* **713**, 816–836.

Newton J., Franchi I. A. and Pillinger C. T. (2000) The oxygen-isotopic record in enstatite meteorites. *Meteorit. Planet. Sci.* **35**, 689–698.

Nishiizumi K., Kohl C. P., Arnold J. R., Klein J., Fink D. and Middleton R. (1991) Cosmic ray produced 10Be and 26Al in Antarctic rocks: exposure and erosion history. *Earth Planet. Sci. Lett.* **104**, 440–454.

Noguchi T., Nakamura T. and Nozaki W. (2002) Mineralogy of phyllosilicate-rich micrometeorites and comparison with Tagish Lake and Sayama meteorites. *Earth Planet. Sci. Lett.* **202**, 229–246.

Pattyn F., Matsuoka K. and Berte J. (2010) Glacio-meteorological conditions in the vicinity of the Belgian Princess Elisabeth Station, Antarctica. *Antarct. Sci.* **22**, 79–85.

Raisbeck G. M., Yiou F., Bourles D. and Maurette M. (1986) ^{10}Be and ^{26}Al in Greenland cosmic spherules: Evidence for irradiation in space as small objects and a probable cometary origin. *Meteoritics* **21**, 487–488.

Rochette P., Folco L., Suavet C., van Ginneken M., Gattacceca J., Perchiazzi N., Braucher R. and Harvey R. P. (2008) Micrometeorites from the Transantarctic Mountains. *Proc. Natl. Acad. Sci. USA* **105**, 18206–18211.

Roeder P. L. and Reynolds I. (1991) Crystallization of chromite and chromium solubility in basaltic melts. *J. Petrol.* **32**, 909–934.

Rubin A. E. (2018) Mechanisms accounting for variations in the proportions of carbonaceous and ordinary chondrites in different mass ranges. *Meteorit. Planet. Sci.* **53**, 2181–2192.

Rubin A. E. and Grossman J. N. (2010) Meteorite and meteoroid: New comprehensive definitions. *Meteorit. Planet. Sci.* **45**, 114–122.

Rudraswami N. G., Parashar K. and Shyam Prasad M. (2011) Micrometer- and nanometer-sized platinum group nuggets in micrometeorites from deep-sea sediments of the Indian Ocean. *Meteorit. Planet. Sci.* **46**, 470–491.

Rudraswami N. G., Shyam Prasad M., Babu E. V. S. S. K., Vijaya Kumar T., Feng W. and Plane J. M. C. (2012) Fractionation and fragmentation of glass cosmic spherules during atmospheric entry. *Geochim. Cosmochim. Acta* **99**, 110–127.

Rudraswami N. G., Shyam Prasad M., Nagashima K. and Jones R. H. (2015a) Oxygen isotopic composition of relict olivine grains in cosmic spherules: Links to chondrules from carbonaceous chondrites. *Geochim. Cosmochim. Acta* **164**, 53–70.

Rudraswami N. G., Shyam Prasad M., Dey S., Plane J. M. C., Feng W. and Taylor S. (2015b) Evaluating changes in the elemental composition of micrometeorites during entry into the Earth's atmosphere. *Astrophys. J.* **814**, 78. https://doi.org/10.1088/0004-637X/814/1/78.

Rudraswami N. G., Shyam Prasad M., Babu E. V. S. S. K. and Vijaya Kumar T. (2016) Major and trace element geochemistry of S-type cosmic spherules. *Meteorit. Planet. Sci.* **51**, 718–742.

Schulze H., Bischoff A., Palme H., Spettel B., Dreibus G. and Otto J. (1994) Mineralogy and chemistry of Rumuruti: The first meteorite fall of the new R chondrite group. *Meteorit. Planet. Sci.* **29**, 275–286.

Scott E. R., Greenwood R. C., Franchi I. A. and Sanders I. S. (2009) Oxygen isotopic constraints on the origin and parent bodies of eucrites, diogenites, and howardites. *Geochim. Cosmochim. Acta* **73**, 5835–5853.

Shiraishi K., Osanai Y., Ishizuka H. and Asami M. (1997) *Geological Map of the Sør Rondane Mountains, Antarctica. Antarctic Geological Map Series, Sheet 35, Scale 1:250,000.* National Institute of Polar Research, Tokyo.

Shiraishi, K., Dunkley, D. J., Hokada, T., Fanning, C. M., Kagami, H. and Hamamoto, T. (2008) Geochronological constraints on the Late Proterozoic to Cambrian crustal evolution of eastern Dronning Maud Land, East Antarctica: a synthesis of SHRIMP U-Pb age and Nd model age data. In Geodynamic Evolution of East Antarctica: A Key to the

East-West Gondwana Connection (eds. M. Satish-Kumar, Y. Motoyoshi, Y. Osanai, Y. Hiroi and K. Shiraishi). Geological Society, London, Special Publications, vol. 308. pp. 21–67.

Shyam Prasad M., Rudraswami N. G. and Panda D. K. (2013) Micrometeorite flux on Earth during the last ~50,000 years. *J. Geophys. Res.-Planet.* **118**, 2381–2399.

Starkey N. A., Franchi I. A. and Lee M. R. (2014) Isotopic diversity in interplanetary dust particles and preservation of extreme 16 O-depletion. *Geochim. Cosmochim. Acta* **142**, 115–131.

Steele A. (1992) Olivine in Antarctic micrometeorites: Comparison with other extraterrestrial olivine. *Geochim. Cosmochim. Acta* **56**, 2923–2929.

Suavet C., Rochette P., Kars M., Gattacceca J., Folco L. and Harvey R. P. (2009) Statistical properties of the Transantarctic Mountains (TAM) micrometeorite collection. *Polar Sci.* **3**, 100–109.

Suavet C., Alexandre A., Franchi I. A., Gattacceca J., Sonzogni C., Greenwood R. C., Folco L. and Rochette P. (2010) Identification of the parent bodies of micrometeorites with high-precision oxygen isotope ratios. *Earth Planet. Sci. Lett.* **293**, 313–320.

Suavet C., Cordier C., Rochette P., Folco L., Gattacceca J., Sonzogni C. and Damphoffer D. (2011a) Ordinary chondrite related giant (>800 μm) cosmic spherules from the Transantarctic Mountains, Antarctica. *Geochim. Cosmochim. Acta* **75**, 6200–6210.

Suavet C., Gattacceca J., Rochette P. and Folco L. (2011b) Constraining the terrestrial age of micrometeorites using their record of the Earth's magnetic field polarity. *Geology* **39**, 123–126.

Suganuma Y., Miura H., Zondervan A. and Okuno J. (2014) East Antarctic deglaciation and the link to global cooling during the Quaternary: evidence from glacial geomorphology and ^{10}Be surface exposure dating of the Sør Rondane Mountains, Dronning Maud Land. *Quat. Sci. Rev.* **97**, 102–120.

Suttle M. D., Folco L., Genge M. J., Russell S. S., Najorka J. and van Ginneken M. (2019) Intense aqueous alteration on C-type asteroids: Perspectives from giant fine-grained micrometeorites. *Geochim. Cosmochim. Acta* **245**, 352–373.

Taylor S. and Brownlee D. E. (1991) Cosmic spherules in the geological record. *Meteoritics* **26**, 203–211.

Taylor S. and Lever J. H. (2001) Seeking unbiased collections of modern and ancient micrometeorites. In *Accretion of Extraterrestrial Matter Throughout Earth's History* (eds. B. Peucker-Ehrenbrink and B. Schmitz). Kluwer Academic/Plenum Publishers, New York, pp. 205–219.

Taylor S., Lever J. H. and Harvey R. P. (1998) Accretion rate of cosmic spherules measured at the South Pole. *Nature* **392**, 899–903.

Taylor S., Lever J. H. and Harvey R. P. (2000) Numbers, types and compositional distribution of an unbiased collection of cosmic spherules. *Meteorit. Planet. Sci.* **35**, 651–666.

Taylor S., Alexander C. M. O., Delaney J. S., Ma P., Herzog G. F. and Engrand C. (2005) Isotopic fractionation of iron, potassium, and oxygen in stony cosmic spherules: Implications for heating histories and sources. *Geochim. Cosmochim. Acta* **69**, 2647–2662.

Taylor S., Herzog G. F. and Delaney J. S. (2007a) Crumbs from the crust of Vesta: Achondritic cosmic spherules from the South Pole water well. *Meteorit. Planet. Sci.* **42**, 223–233.

Taylor S., Matrajt G., Lever J. H., Joswiak D. J. and Brownlee D. E. (2007b) Size distribution of Antarctic micrometeorites. In *Workshop on Dust in Planetary Systems* (eds. H. Krueger and A. Graps). ESA, NY, pp. 145–148.

Taylor S., Matrajt G. and Guan Y. (2012) Fine-grained precursors dominate the micrometeorite flux. *Meteorit. Planet. Sci.* **47**, 550–564.

Thiemens M., Jackson T., Zipf E., Erdman P. W. and Van Egmond C. (1995) Carbon dioxide and oxygen isotope anomalies in the mesosphere and stratosphere. *Science* **270**, 969–972.

van Ginneken M., Folco L., Perchiazzi N., Rochette P. and Bland P. A. (2010) Meteoritic ablation debris from the Transantarctic Mountains: Evidence for a Tunguska-like impact over Antarctica ca. 480 ka ago. *Earth Planet. Sci. Lett.* **293**, 104–113.

van Ginneken M., Folco L., Cordier C. and Rochette P. (2012) Chondritic micrometeorites from the Transantarctic Mountains. *Meteorit. Planet. Sci.* **47**, 228–247.

van Ginneken M., Genge M. J., Folco L. and Harvey R. P. (2016) The weathering of micrometeorites from the Transantarctic Mountains. *Geochim. Cosmochim. Acta* **179**, 1–31.

van Ginneken M., Gattacceca J., Rochette P., Sonzogni C., Alexandre A., Vidal V. and Genge M. J. (2017) The parent body controls on cosmic spherule texture: Evidence from the oxygen isotopic compositions of large micrometeorites. *Geochim. Cosmochim. Acta* **212**, 196–210.

Van Roosbroek N., Debaille V., Pittarello L., Goderis S., Humayun M., Hecht L., Jourdan F., Spicuzza M. J., Vanhaecke F. and Claeys Ph. (2015) The formation of IIE iron meteorites investigated by the chondrule-bearing Mont Dieu meteorite. *Meteorit. Planet. Sci.* **50**, 1173–1196.

Vlassenbroeck J., Dierick M., Masschaele B. C., Cnudde V., Van Hoorebeke L. and Jacobs P. (2007) Software tools for quantification of X-ray microtomography at the UGCT. *Nucl. Instrum. Meth. A* **580**, 442–445.

Wang J., Davis A. M., Clayton R. N., Mayeda T. K. and Hashimoto A. (2001) Chemical and isotopic fractionation during the evaporation of the FeO–MgO–SiO_2–CaO–Al_2O_3–TiO_2–REE melt system. *Geochim. Cosmochim. Acta* **65**, 479–494.

Welten K. C., Folco L., Nishiizumi K., Caffee M. W., Grimberg A., Meier M. M. M. and Kober F. (2008) Meteoritic and bedrock constraints on the glacial history of Frontier Mountain in northern Victoria Land, Antarctica. *Earth Planet. Sci. Lett.* **270**, 308–315.

Yada T., Nakamura T., Takaoka N., Noguchi T., Terada K., Yano H., Nakazawa T. and Kojiima H. (2004) The global accretion rate of extraterrestrial materials in the last glacial period estimated from the abundance of micrometeorites in Antarctic glacier ice. *Earth Planets Space* **56**, 67–79.

Yada T., Nakamura T., Noguchi T., Matsumoto N., Kusakabe M., Hiyagon H., Ushikubo T., Sugiura N., Kojima H. and Takaoka N. (2005) Oxygen isotopic and chemical compositions of cosmic spherules collected from the Antarctic ice sheet: Implications for their precursor material. *Geochim. Cosmochim. Acta* **69**, 5789–5804.

Zekollari H., Goderis S., Debaille V., van Ginneken M., Gattacceca J., ASTER Team, Jull A. J., Lenaerts J., Yamaguchi A., Huybrechts Ph. and Claeys Ph. (2019) Unravelling the high-altitude Nansen blue ice field meteorite trap (East Antarctica) and implications for regional palaeo-conditions. *Geochim. Cosmochim. Acta* **248**, 289–310.

Associate Editor: Rhian Jones